Development of *In-Situ* Plasma Processing on 1.3 GHz Superconducting Radiofrequency Cavities at TRIUMF

by

Daniel Hedji
B.Sc., University of Victoria, British Columbia, 2022

A Thesis Submitted in Partial Fulfillment of the
Requirements for the Degree of

MASTER OF SCIENCE

in the Department of Physics and Astronomy

We acknowledge and respect the Lək̓ʷəŋən (Songhees and Xʷsepsəm/Esquimalt) Peoples on whose territory the university stands, and the Lək̓ʷəŋən and W̱SÁNEĆ Peoples whose historical relationships with the land continue to this day.

Development of *In-Situ* Plasma Processing on 1.3 GHz Superconducting Radiofrequency Cavities at TRIUMF

by

Daniel Hedji
B.Sc., University of Victoria, British Columbia, 2022

Supervisory Committee

Robert Laxdal, Co-Supervisor
(Department of Physics and Astronomy)

Dr. Tobias Junginger, Co-supervisor
(Department of Physics and Astronomy)

ABSTRACT

Superconducting Radio Frequency (SRF) technology is a key component in many particle accelerators operating in a continuous wave, or high duty cycle, mode. The on-line performance of SRF cavities, as defined by the accelerating gradient and the unloaded quality factor, Q_0, is negatively impacted by the gradual increase of particulate contamination, furthering field emission. Conventional cleaning procedures are both time- and resource-exhaustive as they are done *ex-situ*. Plasma processing is an emerging *in-situ* method of cleaning which chemically removes hydrocarbon-based field emitters by the ignition of a plasma in the cavity volume. An R&D program is underway at TRIUMF with the goal of developing fundamental power coupler (FPC) driven plasma processing of the installed 1.3 GHz nine-cell cavities in the ARIEL 30 MeV SRF eLINAC.

Processing recipes have been systematically studied in one single-cell and two multi-cell cavities off-line. Cavities were first artificially contaminated using a Helium-Methane plasma. In most of the tests, the removal of hydrocarbons was verified through the byproduct responses on a Residual Gas Analyzer (RGA). A plasma recipe with a cavity pressure of 80 mTorr, and a gas ratio of 95% Helium to 5% Oxygen was found to remove the largest abundances of hydrocarbon byproducts from each of the tested cavities. Cavity performance changes were tested cryogenically before and after conditioning with this particular recipe. These experiments were unable to recover the cavity performance but did provide insight toward the plasma processing testing procedure and apparatus needed for assembled cavities.

Multi-cell testing was also conducted to identify plasma locations for the various modes in the fundamental TM_{010} passband. Here, a predictive model was developed to compare frequency shift data resulting from a plasma ignition with field behavior collected from beadpull distributions through a least-squares minimization. The results presented show the estimated plasma locations and movements due to power increases.

Contents

List of Tables

List of Figures

ACKNOWLEDGMENTS

I would like to recognize several individuals who have supported and guided me throughout the course of this thesis. The support and guidance they provided meant more than they could imagine. This work would not have been possible otherwise.

Firstly, I am incredibly grateful for my TRIUMF supervisors: Bob, Philipp, Yao, and Vladimir. Bob, the guidance you provided shaped me into the scientist I am. The insight, experience, and ambition you displayed was invaluable. You gave me the motivation I needed to grow as a student. To Philipp, thank you for fostering my scientific curiosity. You always took the time to answer my questions or teach me something new. I will always use the skills and tips you provided me. Yao, the discussions we had challenged my thinking. By doing so, you allowed me to consider new perspectives, building my confidence in my approaches. Vladimir, thank you for sharing your expertise on RF with me. The explanations you gave helped me understand the laboratory environment immensely.

To Tobi, you took a chance on me for undergrad research. You inspired me to continue with physics and aided me in obtaining this graduate position. Each of my steps in academia has had you guiding me. Your insight and experience has helped me develop as a researcher and I cannot thank you enough.

I also want to thank my lifelong friends, Arshdeep, Campbell, Noah, Sean, Liam, Liam, Maeve, Paolina, Evan, and Kieran, for the companionship you have provided me. We have been through thick and thin together, and I would not be the man I am today without all you.

To those from UVic, Aydan, Scott, Noah, Jenna, Nicola, and Linzhi. I largely attribute my success in undergraduate and graduate studies to the examples you set. Your work ethic pushed me out of my comfort zone and taught me that I could achieve anything I set my mind to. I have never met people more dedicated and smart. I know that wherever life takes you, each of you will find success.

To my Vancouver friends, Mallory, Annabelle, Alex, Serene, Wilfred, and Jackie. I would thank you guys, but I don't want to give you that satisfaction. In all seriousness, you guys made me feel at home in a new city. The memories we made will always be cherished, so thank you.

For Patrick, Anna, and Monika, thank you for constantly believing in me and encouraging me to go beyond what I thought I was capable of.

To my parents, Denis and Suzana, thank you for the unending support you have provided to me throughout my life. Without you, I would not have the resilience, curiosity, or dedication to have reached this point. This thesis reflects the hard work and sacrifices you made to raise us.

And to my Celina, I don't think words can fully describe how much I love you. You continue to push me to be the best version of myself in a way no one else can. I hope I have made you proud; this thesis is yours as much as it is mine. Thank you for being there for me, and I can't wait to enter this next chapter of my life with you.

DEDICATION

To my parents, hvala ti za sve.

Chapter 1

Introduction

Over the past century, particle accelerators have become a cornerstone in many scientific and industrial applications. Accelerators use electric fields to propel charged particles to higher velocities, enabling particle discovery research, cancer irradiation techniques, and ion implantation in semiconductor fabrication, among others. At TRIUMF, particle accelerators are used to create Rare Isotope Beams (RIBs). The ISAC (Isotope Separator and ACcelerator) facility creates exotic nuclei by bombarding thick high-power targets with a 500 MeV proton beam from its cyclotron [1]. RIB's are then delivered to one of three areas to support various physics experiments.

To supplement RIB production and simultaneously provide three RIBs, TRIUMF's Advanced Rare IsotopE Laboratory (ARIEL) program was developed [2]. ARIEL includes a 3 mA, 30 MeV SRF electron linear accelerator (eLINAC) that operates in a continuous-wave (cw) mode to accelerate electron beams into a converter target to produce Bremsstrahlung X-rays. X-rays produced from the initial reaction are then incident onto Actinide targets, which, through photofission processes, form radioactive species [3].

ARIEL's eLINAC consists of three 1.3 GHz nine-cell elliptical Superconducting RadioFrequency (SRF) cavities that are housed across two cryomodules; one within an injector cryomodule, and two within the remaining accelerating cryomodule. Each cryomodule is designed to maintain temperatures near absolute zero to maintain the cavity's superconducting state. While cooled, the SRF cavities are exceptionally efficient at acceleration, exhibiting surface resistances that are in the nΩ range. SRF cavities in ARIEL are all specified to operate at a minimum gradient of 10 MV/m to achieve a threshold RIB energy production energy of 30 MeV [4].

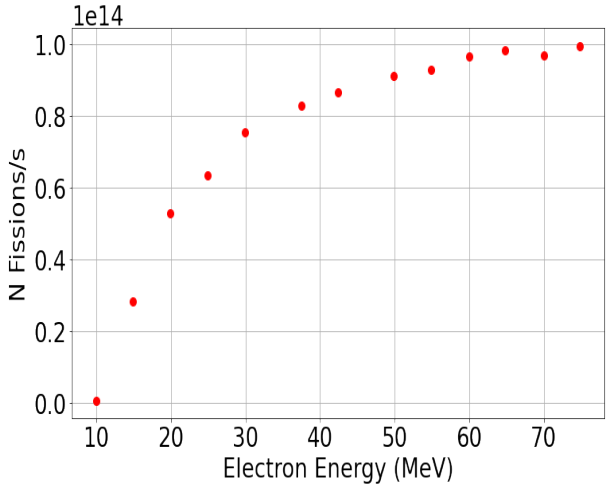

Figure 1.1: Number of photo-fissions produced as a function of electron energy for the ARIEL target stations [5]. Currently, ARIEL is designed to operate at 30 MeV.

The photofission process used to generate RIBs is highly dependent on the incident electron energy, as can be seen in Figure 1.1. The yield of fissions strongly increases with the electron beam energy up to 30 MeV, eventually saturating around 50 MeV. Field emission induced by particulate contamination poses a serious concern to ARIEL's experimental efficiency. Field emission refers to the emission of electrons typically from contamination by the RF field. These electrons are accelerated by the cavity fields and hit nearby walls, creating bremsstrahlung X-rays. The additional power losses introduced by the electrons degrades the quality factor, limiting the achievable gradient due to high radiation levels and increased cryogenic load. If any of the SRF cavities present in ARIEL experience significant field emission, they will not reach the specified 10 MV/m. As a result, RIB production will suffer.

Several techniques have been developed to reverse field emission contamination. Prior to cavity assembly, high-purity water is sprayed on the inner cavity surface to remove particulates from the cavity walls. Conventionally, this is referred to as High Pressure Rinsing (HPR) [6]. Field emission may also arise during cavity operation. In these cases, RF conditioning or Helium conditioning can be used. RF conditioning is done by increasing the electric field at emitter locations, eventually destroying the emitter [7]. In contrast, helium conditioning aims to bombard emitters using Helium atoms, either sputtering the emitter and destroying it, or creating gas desorption on the emitter [8]. Each of these mentioned techniques can be used to recover the cavity performance in ARIEL. However, if field emission resulting from hydrocarbon contamination is seen, these techniques suffer from some intrinsic limitation.

Specifically, HPR is done *ex-situ* and would require cryomodule disassembly. This process requires a large resource allocation, in addition to presenting long experimental downtimes. Furthermore, both RF conditioning and Helium conditioning cannot adequately remove hydrocarbon field emission. As such, techniques that remove hydrocarbon contamination that can also be performed *in-situ* are quite attractive.

The work presented in this thesis focuses on one such *in-situ* cleaning technique known as plasma processing. Plasma processing specifically targets hydrocarbon field emitters within SRF cavities by sustaining a glow discharge composed of a mixture of an inert and a reactive gas. Ionized Oxygen molecules bond to broken hydrocarbon chains, forming volatile byproducts, which can then be removed from the cavity environment, effectively cleaning the cavity of contaminants.

Plasma processing was initially introduced at the Spallation Neutron Source (SNS) to clean their 805 MHz, high-β cavities using a superposition of modes in the fundamental bandpass [9, 10, 11]. It is now more common to use a superposition of Higher-Order Modes (HOMs) through a HOM coupler to ignite plasma. This technique was first implemented on 9-cell 1.3 GHz Linac Coherent Light Source II (LCLS II) cavities by Fermi National Accelerator Laboratory (FNAL) [12, 13]. TRIUMF is currently pursuing plasma processing for implementation onto the eLINAC to derisk the potential of field emission compromising the RIB yield.

The design of the cryomodules in the eLINAC limits the modes available for plasma processing. HOM dampers are placed at upstream and downstream locations to absorb HOMs. Only the fundamental and first-dipole passbands (see Figure 1.2) are seen to have a sufficient transmission, exhibiting clear resonances above the noise seen at -140 dB. In addition, the 1.3 GHz 9-cell ARIEL cavities are a unique variant of the TESLA design [14], with modified end groups equipped with two Fundamental Power Couplers (FPCs) each [15]. For these reasons, this thesis will explore plasma ignition using FPCs in the TM_{010} passband. Studies performed are aimed at developing a plasma ignition sequence that will clean each cell in the on-line ARIEL cavities successively.

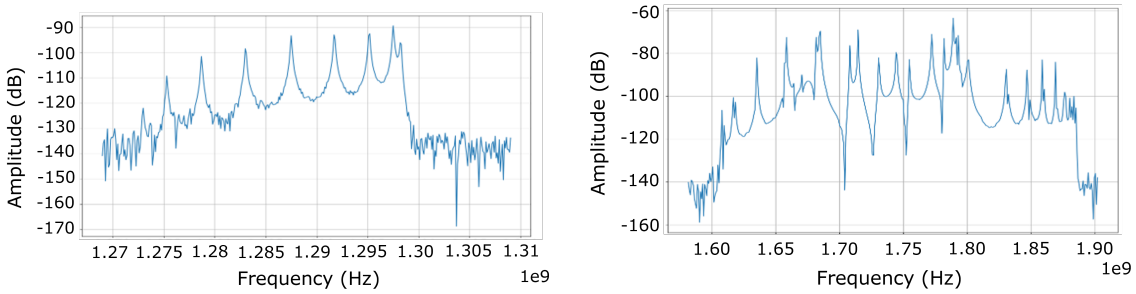

(a) Fundamental TM_{010} passband

(b) First Dipole Passband

Figure 1.2: Transmission measurements of the fundamental TM_{010} and first-dipole passbands from the EINJ injector cryomodule.

1.1 Thesis Organization

The remainder of the thesis is outlined as follows:

Chapter 2 starts by providing the relevant theory behind SRF cavities and degrading phenomena to provide context into how cavity performance is measured and affected. This chapter concludes with an introduction to plasma, discussing important parameters and their role in processing.

Chapter 3 describes the techniques and apparatuses used to perform studies on three 1.3 GHz elliptical cavities. The chapter is categorized by the type of experiment being conducted. The classification is as follows: beadpull measurements and tuning, plasma processing, and cryogenic cold tests.

Chapter 4 presents the experimental results found from the studies described in Chapter 3. In order, these sections are summarized as: multi-cell beadpull distributions before and after tuning, plasma investigations in single-cell and multi-cell structures, and cryogenic RF tests before and after plasma processing to validate gradient restoration. Furthermore, each section discusses the implications of the determined results towards the on-line application of plasma processing.

Chapter 5 concludes the thesis. The findings presented in the previous chapters are highlighted here, together with any recommendations for future studies of plasma processing that will enable the implementation of plasma processing on the ARIEL eLINAC.

Chapter 2

Background

2.1 Resonant Cavities

The concept of resonance is a well-studied phenomenon that can be found in a multitude of every day examples. Resonance describes a matching of oscillation frequencies between a driving force and the natural frequency of a system creating a net amplitude increase. In particle accelerators, RF cavities utilize resonance to accelerate particle beams by resonating at a certain frequency. The response created by the cavity produces electromagnetic field distributions that are designed to align with charged particle trajectories and synchronized to the arrival of charged particle bunches. In this section, a broad overview of the theory behind the working principles of RF and SRF cavities within accelerators will be provided, along with any limitations they may encounter.

2.1.1 Charged Particle Acceleration

When charged particles interact with electromagnetic fields, they experience an accelerating force in the direction of the electric field and a deflecting force from the magnetic field. This effect is known as the Lorentz force and is analytically given by

$$\bar{\mathbf{F}} = q(\bar{\mathbf{E}} + \bar{\mathbf{v}} \times \bar{\mathbf{B}}) \tag{2.1}$$

where $\bar{\mathbf{F}}$ is the accelerating force, $\bar{\mathbf{E}}$ and $\bar{\mathbf{B}}$ are the electric and magnetic fields, $\bar{\mathbf{v}}$ is the instantaneous velocity of the charged particle, and q is the charge of the traveling particle. RF cavities are designed to utilize this principle by creating strong electric fields on the beam axis to accelerate the charged particles.

2.1.2 Resonant Modes

RF cavities are fabricated from electrically conductive material, which, when exposed to incident RF signals, will elicit an electromagnetic response to satisfy the boundary conditions of a conductor. The shape of a resonant cavity determines the produced field patterns within the inner cavity volume. The exact field configuration is dependent on certain boundary conditions, which for wave-guides and cavities, are given by

$$\hat{n} \times \bar{\mathbf{E}} = 0 \tag{2.2}$$

and

$$\hat{n} \cdot \bar{\mathbf{B}} = 0 \tag{2.3}$$

where $\hat{n}$ is the unit vector normal to the cavity wall surface [16].

The electromagnetic field distribution within a resonant cavity can be found by solving the wave equation produced through Maxwell's equations. To begin, Maxwell's equations

$$\bar{\nabla} \cdot \bar{\mathbf{E}} = 0 \tag{2.4}$$

$$\bar{\nabla} \times \bar{\mathbf{E}} = \frac{\partial \bar{\mathbf{B}}}{\partial t} \tag{2.5}$$

$$\bar{\nabla} \cdot \bar{\mathbf{B}} = 0 \tag{2.6}$$

$$\bar{\nabla} \times \bar{\mathbf{B}} = \mu_0 \epsilon_0 \frac{\partial \bar{\mathbf{E}}}{\partial t} \tag{2.7}$$

must be rearranged such that the individual field equations form

$$(\nabla^2 - \frac{1}{\mu_0 \epsilon_0} \frac{\partial^2}{\partial t^2}) \begin{Bmatrix} \bar{\mathbf{E}} \\ \bar{\mathbf{B}} \end{Bmatrix} = 0 \tag{2.8}$$

with t corresponding to time, and μ_0 and ϵ_0 being the permeability and permittivity of free space, respectively [16, 17].

The behavior of $\bar{\mathbf{E}}$ and $\bar{\mathbf{B}}$ is also known. By recalling that the signal input into the cavity is an electromagnetic plane wave in the form of radio-frequency, a generalized ansatz can be provided for each field:

$$\bar{\mathbf{E}}(r, t) = \bar{\mathbf{E}}_0(r, \phi) e^{i(kz - \omega t)} \tag{2.9}$$

$$\bar{\mathbf{B}}(r,t) = \bar{\mathbf{B}}_0(r,\phi)e^{i(kz-\omega t)}. \tag{2.10}$$

Here ω is the angular frequency, and k is the wave number. Additionally, the Laplacian operator, ∇^2, when written in a cylindrical basis, can be expressed as

$$\nabla^2 = \frac{1}{r}\frac{\partial}{\partial r}(r\frac{\partial}{\partial r}) + \frac{1}{r^2}(\frac{\partial^2}{\partial \phi^2}) + \frac{\partial^2}{\partial z^2}. \tag{2.11}$$

Substituting the field equations (2.9) and (2.10) into (2.11), the t and z operators can be solved directly, while the remaining operators are limited through $\bar{\mathbf{E}}_0$ and $\bar{\mathbf{B}}_0$. If these expressions are temporarily left unsolved, (2.8) can be rewritten into

$$\nabla_\perp^2 + (\frac{\omega^2}{\mu_0\epsilon_0} - k^2)\begin{Bmatrix}\bar{\mathbf{E}}\\ \bar{\mathbf{B}}\end{Bmatrix} = 0 \tag{2.12}$$

where $\nabla_\perp$ refers to the components of the Laplacian that cannot be directly found, namely the radial and azimuthal elements; this can otherwise be labeled as the transverse components.

In sharing the same form of differential equation, each respective field must adhere to the boundary conditions set through Equations (2.2) and (2.3). Due to the inherent geometric implications between the two boundary conditions, two families of modes are produced. These can be further classified as the Transverse Magnetic (TM) modes and the Transverse Electric (TE) modes. In TM modes, the field orientation is such that the magnetic fields are purely transverse, while some longitudinal component of the electric field exists. Conversely, the TE modes exhibit electric fields entirely in the transverse plane, while the magnetic field now has a component in the longitudinal plane.

2.1.3 Cavity Structures

Typically linear accelerators are made from several RF cavities that each synchronize their accelerating fields to the arrival of charged particle bunches. There are several RF cavity structures that are designed to operate over a certain particle velocity range. The cavities studied in this thesis, 1.3 GHz elliptical cavities, are designed to accelerate relativistic electrons. In this subsection, descriptions of the elliptical cavity design are presented.

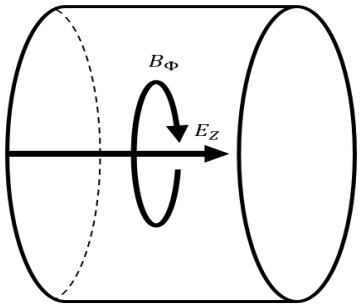

Figure 2.1: Illustration of the pillbox cavity. Longitudinal electric field components are aligned along the beam axis, while magnetic field components are visualized azimuthally.

The Pill-Box Cavity

One RF cavity known as the "pill-box" cavity has a simple geometry that allows for exact analytic field expressions. Shown in Figure 2.1, the pill-box cavity is a cylindrical cavity that is suited for accelerating on-axis particle beams longitudinally using TM modes.

The generalized set of TM modes for the pill-box cavity of length L and radius R are presented below. The subscripts m, n, and p denote the integer number of sign changes the longitudinal electric field, E_z, undergoes in the ϕ, ρ, and z directions, respectively [18].

$$E_z = E_0 \cos(\frac{\pi p z}{L}) J_m(\frac{x_{mn} r}{R}) \cos(m\phi) \tag{2.13}$$

$$E_r = -E_0 \frac{\pi p R}{L x_{mn}} \sin(\frac{\pi p z}{L}) J'_m(\frac{x_{mn} r}{R}) \cos(m\phi) \tag{2.14}$$

$$E_\phi = E_0 \frac{\pi m p R^2}{r L x_{mn}^2} \sin(\frac{\pi p z}{L}) J_m(\frac{x_{mn} r}{R}) \sin(m\phi) \tag{2.15}$$

$$B_z = 0 \tag{2.16}$$

$$B_r = iE_0 \frac{m\mu_0 \omega_{mnp} R^2}{\eta c r x_{mn}^2} \cos(\frac{\pi p z}{L}) J_m(\frac{x_{mn} r}{R}) \sin(m\phi) \tag{2.17}$$

$$B_\phi = iE_0 \frac{\mu_0 \omega_{mnp} R}{\eta c x_{mn}} \cos(\frac{\pi p z}{L}) J'_m(\frac{x_{mn} r}{R}) \cos(m\phi) \tag{2.18}$$

Here x_{mn} is the n^{th} root of the Bessel's function J_m, or its derivative J'_m, η represents the impedance of free space, which has a value of approximately 377 Ω, and ω_{mnp} is the resonant frequency associated with the operating mode. The value ω_{mnp} is calculated through the

relation

$$\omega_{mnp} = c\sqrt{(\frac{x_{mn}}{R})^2 + (\frac{\pi p}{d})^2}. \tag{2.19}$$

Many of the potential pill-box modes cannot adequately accelerate particle beams longitudinally as the electric field will vanish at some point along the beam axis. Consequently, TM_{0n0} modes are typically chosen for acceleration. A common choice amongst the accelerating modes is the TM_{010} mode, otherwise known as the fundamental mode for cavities with $R/L < 2$, as it has the smallest size for a particular frequency, comparatively [18]. Analytic estimation of the frequency of the TM_{010} mode is done using

$$\omega_{010} = \frac{2.405c}{R}. \tag{2.20}$$

Within the set of TM modes, there are other solution sets that more suited for other aspects of beam transport. For example, TM_{1np} modes, conventionally known as dipole modes, are typically chosen for beam deflection.

To be useful for acceleration, the length of a pillbox cavity has to be limited such that the particle transit time through the cavity is no more than a half-period of the RF cycle. For speed of light particles, this occurs when $L = \frac{\lambda}{2}$.

Elliptical Cavities

Early SRF cavities were made from multiple pill-box cells coupled together. It was found that the geometry was prone to strong multipacting (see Section 2.1.6.) and so the design was modified to an elliptical shape [19]. The resulting design is now known as the elliptical cavity.

Shown on the left-hand side of Figure 2.2 is an example of a superconducting elliptical cavity. The elliptical cavity displayed is a TESLA design [14] and has nine elliptical segments that each correspond to a single-cell. Each cell is composed of two half-cells that are welded together at the largest radius region known as the equator. Two half-cells form a single-cell cavity that can accelerate particle beams in the TM_{010} mode. To increase accelerating efficiency, many cells are attached in series to form a multi-cell cavity. With 1.3 GHz cavities, the most common choice for the number of cells is nine. Active acceleration will vary depending on the speed of the incident beam. The elliptical cavity shown in Figure 2.2 is designed to accelerate particles traveling near the speed of light, which, for electrons, occurs at fairly low kinetic energies [7]. Within ARIEL, electrons effectively travel at $\beta =$

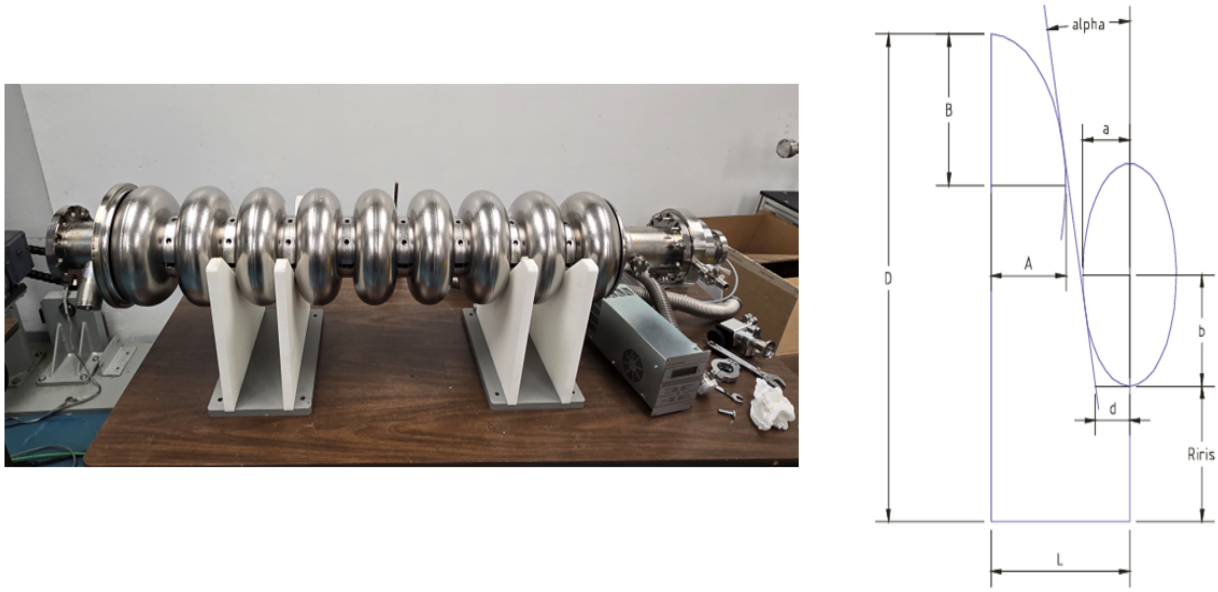

Figure 2.2: Pictured on the left is a 1.3 GHz TESLA elliptical 9-cell SRF cavity. The TESLA variant displays a unique feature in that two end groups are centered along the beam axis, with HOM ports being located nearby on transverse axes. On the right is a graphic of the elliptical cavity shape parametrization. Schematic taken from [20].

1. To estimate the ideal cell length for particle beams moving at this speed, the relation

$$L = \beta \frac{\lambda}{2} \tag{2.21}$$

is used. Here the wavelength, λ, is further given by

$$\lambda = \frac{2\pi c}{\omega}. \tag{2.22}$$

For the TM_{010} mode, the electromagnetic field configurations within elliptical cavities follow trends similar to those found in the pill-box. In particular, the orientation of the electric field is highest along the beam axis of the cavity, with the field amplitude decreasing as a function of radial distance. Magnetic fields, on the other hand, are the strongest around the cell's equator, in which they follow a curled path.

To enable energy flow between the individual cells, cells are coupled to one another to form a multi-resonator array. With a given number of cells, there will be an equal amount of modes produced for each resonance, all possessing a unique frequency, cell field amplitude, and field distribution [21]. This cluster of modes is conventionally labeled as a passband.

Due to their acceleration specifications, elliptical cavities are typically operated using the fundamental, or TM_{010}, passband. However, the distinctive behaviors of the passband modes are not all suitable for acceleration due to the unequal electric field strength in each cell. The last mode in the passband, the "π-mode", has equal field amplitude in each cell with a π degree phase shift between cells. The periodicity of the field polarization change is set to match half of an RF cycle corresponding to the time of flight from one cell to the next by the particle beam. In this way, the particle beam remains synchronized to the peak of the electric field at the center of each cell, acquiring maximal acceleration.

2.1.4 Figures of Merit

Figures of merit are a set of parameters that describe some operational aspect of RF or SRF cavities. This section introduces key figures of merit that will be relevant to this study.

Quality Factor

The first figure of merit to be introduced is the power dissipation, P_c. When exposed to alternating currents, conductive material will allow surface currents to flow in a thin layer to sustain the produced electromagnetic fields. Ohmic power losses form as a result of the resistive properties of the material chosen [18]. To quantify this, P_c can be calculated over the surface of the cavity using

$$P_c = \frac{1}{2}\int R_s |\bar{\mathbf{H}}|^2 ds \tag{2.23}$$

where R_s represents the RF surface resistance, s is the surface variable, and $\bar{\mathbf{H}}$ is the magnitude of the local magnetic field.

The unloaded quality-factor, Q_0 is defined as the ratio of the stored energy to the energy lost per radian of the RF cycle. In its most general form, Q_0 is given by

$$Q_0 = \frac{\omega_0 U}{P_c} \tag{2.24}$$

where U is the stored energy in the cavity. For a given field strength, the total stored energy is a constant, but individual components fluctuate between the electric and magnetic field components. Therefore U can be found using

$$U = \frac{1}{2}\mu_0 \int_V |\bar{\mathbf{H}}|^2 dv = \frac{1}{2}\epsilon_0 \int_V |\bar{\mathbf{E}}|^2 dv \tag{2.25}$$

where V is the volumetric term, and v is its integrand placeholder. Assuming a constant surface resistance across the cavity surface, a quick substitution of Equations (2.23) and (2.25) into Equation (2.24) yields

$$Q_0 = \frac{\mu_0 \omega_0 \int_V |\bar{\mathbf{H}}|^2 dv}{R_s \int |\bar{\mathbf{H}}|^2 ds} = \frac{G}{R_s} \tag{2.26}$$

where G here is referred to as the geometry factor. What can immediately be seen with the behavior of G is that it depends on the volume and surface integrals. In other words, G is dependent only on the cavity geometry and not on the size of the cavity. Equation (2.26) implies that R_s must be minimized to maximize Q_0.

External Quality Factor and Coupling

Each component added to the cavity will produce a unique power loss rate, P_e, based on how much energy will leave the system through it. Power couplers that feed RF to the cavity or pick-up couplers that sample the field are some examples of sources of power loss. By normalizing P_e to the stored energy within the cavity, the original definition of Q can be reapplied to measure the "external losses" due to a specific component. Commonly, this quantification is known as the external quality factor (Q_{ext}) and is given by

$$Q_{ext} = \frac{\omega_0 U}{P_e}. \tag{2.27}$$

Each contributing component can also be combined into one overarching term, the loaded quality factor, Q_L, that encapsulates the overall losses seen by the cavity. Similar to (2.27), Q_L can be written as

$$Q_L = \frac{\omega_0 U}{P_{tot}}. \tag{2.28}$$

where P_{tot} is the total power loss in the cavity and is given by

$$P_{tot} = P_c + P_{e1} + P_{e2} + ... \tag{2.29}$$

where P_{e1} is the power loss due to component one, and so forth. Expanding (2.28) using (2.29) yields

$$\frac{1}{Q_L} = \frac{1}{Q_0} + \frac{1}{Q_{ext1}} + ... \tag{2.30}$$

To further characterize the coupling between the cavity and a component, the coupling factor, β can be used. β is defined to be the ratio of the unloaded quality factor to the

loaded quality factor, i.e.

$$\beta = \frac{Q_0}{Q_{ext}}, \tag{2.31}$$

which gives

$$Q_0 = Q_L(1 + \beta) \tag{2.32}$$

when applied into (2.30). The values of β can be divided into three categories: undercoupled ($\beta < 1$), critically coupled ($\beta = 1$), and overcoupled ($\beta > 1$).

Accelerating Gradient

Cavity-to-beam energy transfer is an alternative method to quantify the performance of accelerating cavities. By using a figure of merit known as the accelerating gradient, comparisons with measured data becomes possible. Denoted as E_{acc}, the accelerating gradient is defined as the maximum energy gain of a charged particle over a cavity length L. In analytic form,

$$E_{acc} = \frac{V_c}{L} \tag{2.33}$$

where V_c refers to the maximum voltage received by an on-axis charged particle and is given through

$$V_c = |\int_0^L E_z(\rho = 0, z) \exp^{\frac{i\omega_0 z}{\beta c}} dz|. \tag{2.34}$$

Peak Fields

The achievable surface fields within a cavity imposes an upper limit to the strength of the accelerating gradient. When greater than the field emission threshold, the peak surface electric field, E_{pk}, can lead to electrical breakdown and increased electron release through field emission (see Section 2.1.6.). The peak surface magnetic field, H_{pk}, for SRF cavities is fundamentally limited to values less than H_{sh}, which for Niobium is in the range of $\sim$ 200-250 mT [22]. If this limit is passed, superconducting cavities will transition into a normal conducting state [18, 23]. Good cavity design includes minimizing the ratios $\frac{E_{pk}}{E_{acc}}$ and $\frac{H_{pk}}{E_{acc}}$, to allow higher accelerating gradients below peak surface field limitations.

2.1.5 Superconductivity

Following the discovery of liquid Helium in 1911, Kamerlingh Onnes conducted an experiment testing the resistance of Mercury at the boiling point of Helium to eventually compare with the findings found at hydrogen temperatures [24]. Onnes noted that at temperatures

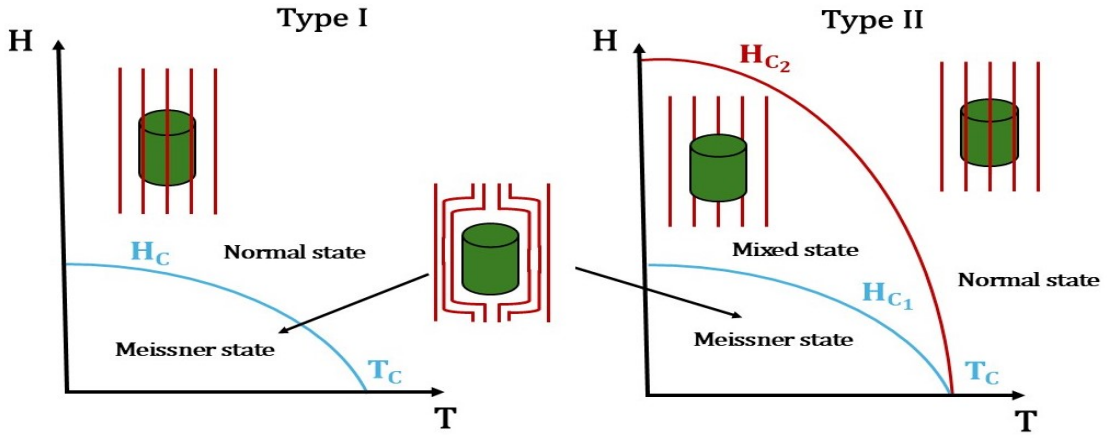

Figure 2.3: Phase diagram for type I (left), and type II (right) superconductors. Here the images of cylinders with surrounding red lines depict the process of flux expulsion. Image inspiration based on [27].

below 4.2K, the electrical resistance of Mercury became so small that it could not be resolved. This phenomena was coined superconductivity. Later in 1933, Meissner and Ochsenfeld reported that this conversion from normal conductivity into superconductivity also forcefully expels magnetic flux if the phase transition occurs in the presence of an external magnetic field [25]; this effect is now formally known as the Meissner effect. Finally, forty years after Onnes' discovery, Bardeen, Cooper, and Schrieffer formulated what is now one of the most prevalent explanations of superconductivity [26]. Their model, BCS theory, microscopically describes superconductivity through a pairing of electrons, known as a Cooper pair. These three discoveries pioneered the study and use of superconductors in various research and industrial applications. Of all superconducting materials, Niobium is the standard choice for the design of SRF cavities as it has the highest critical magnetic field, along with good malleability and a high transition temperature, T_c, of 9.2 K. This section will briefly highlight important aspects of superconductors and their associated theory.

Superconductors can be classified as type I or type II. Type I superconductors generate an equal, yet opposite, magnetization to exactly cancel the applied field up until a critical magnetic field, H_c, is reached. Once the critical field is crossed, the normal conducting state will become more energetically favorable and the Meissner state, as a consequence, will be broken. Type II superconductors differ from type I superconductors in that they are characterized by two critical magnetic fields, H_{c1} and H_{c2}. A relevant example of a type II superconductor is Niobium. Type I and type II superconductors are indistinguishable when the applied field is lower than H_c or H_{c1}, as both will be in a complete Meissner state. How-

ever, once the applied field is between H_{c1} and H_{c2}, type II superconductors enter a "vortex" state. In a vortex state, magnetic flux begins to penetrate into the material, creating normal conducting zones. Any field that surpasses H_{c2} will transition the superconductor into a normal conducting material. SRF cavities must be run while in the Meissner state. Otherwise, flux moving underneath the RF field will add another dissipation outlet. A summary illustration of these two effects can be seen in Figure 2.3.

At zero field and $T = T_c$, the conducting material enters a superconducting state, and the microscopic behavior will evolve from a classical description of a conductor into the quantum mechanical representation of a superconductor, as predicted by BCS theory. In BCS theory, electrons with opposite spin and momentum can be bound to each other through the mediation of phonon wakes. Phonon wakes are created by distortions in the atomic lattice from the movement of negatively charged conduction electrons. The resulting positive charge accumulation will act on a neighboring electron, which, in turn, will create the electron pair, otherwise labeled the Cooper pair. The formation of Cooper pairs will redistribute the available bound states, creating a material-dependent energy gap of $2\Delta(\mathrm{T})$ between a newly formed superconducting ground state and the excited states.

Between T_c and absolute zero, normal electrons and Cooper-paired electrons coexist. Often compared to fluids, these electrons will fall into an isolated, "free" electron fluid, or will pair with another electron to form a Cooper pair and carry current with no resistance [18]. Both fluids flow parallel to one another, but only the superfluid will have an active current-carrying role, as it is the path of least resistance. The ratio between the two fluids is temperature dependent, with all electrons being paired into Cooper pairs at $T = 0$. Conversely, at $T = T_c$, all electrons will be in a free, unpaired state. The relation describing the number of normal electrons, n_{normal}, as a function of temperature is given by

$$n_{normal} \propto \exp\left(-\frac{\Delta}{k_B T}\right) \tag{2.35}$$

where k_B here is the Boltzmann factor. Unlike the Direct Current (DC) case, applying RF into an SRF cavity will produce a finite surface resistance. The inertia of the Cooper pair prevents a full screening of the applied field, allowing a time-varying electric field to penetrate into normal electrons, providing an accelerating and decelerating effect that creates surface dissipation. The direct correlation between normal electrons and the resistance produced requires that the total surface resistance follows a trend similar to that seen in (2.35). The

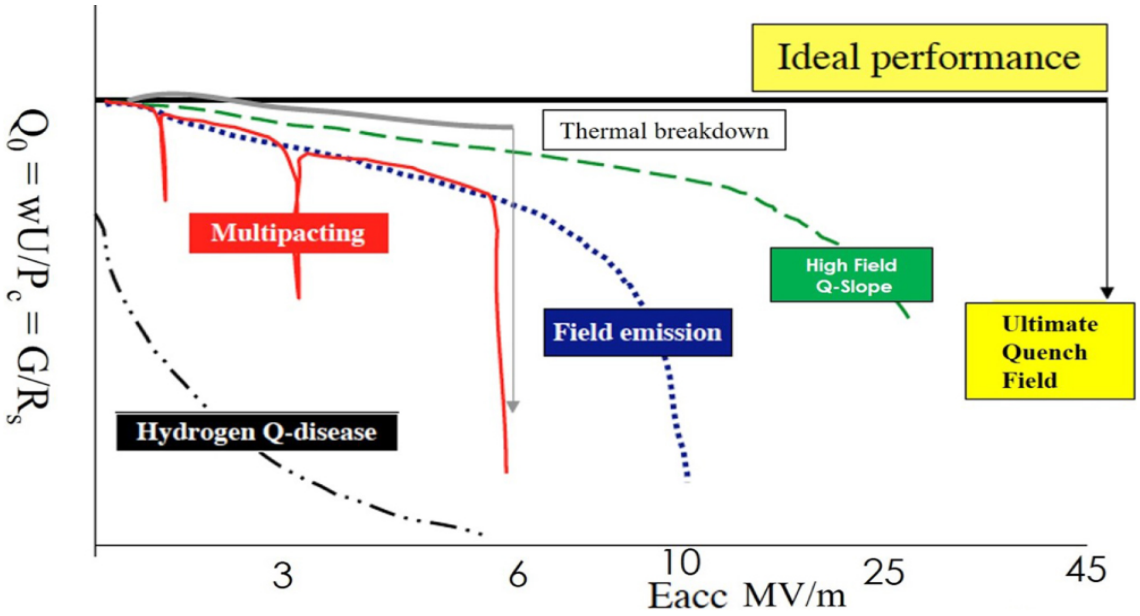

Figure 2.4: Q_0 vs. E_{acc} curves for various degrading effects. Included is the idealized performance of Niobium, which ends at the theoretical material limit at approximately 45 MV/m. Reproduced from [7] under fair use.

total surface resistance produced can be expressed as

$$R_s = A_s \frac{\omega^2}{T} \exp\left(-\frac{\Delta(0)}{k_B T}\right) \tag{2.36}$$

where A_s is a constant that is determined through material parameters like the mean free path of electrons. Experimental measurements show that R_s drops exponentially with temperature until a constant minimum is reached. This residual resistance originates from multiple sources, such as: surface defects, oxide formation on the material surface, and trapped magnetic flux. To account for each source of resistance addition, an overarching term known as the residual is added to (2.36). In analytic form,

$$R_s = R_{BCS} + R_0 \tag{2.37}$$

where R_{BCS} is the resistance predicted by Equation (2.36), and R_0 is the residual resistance.

2.1.6 Performance Limitations of SRF Cavities

Cost is a primary consideration in accelerator design globally. Currently, a major driver of the operating expense associated with SRF cavity implementation is with maintaining

cryogenic temperatures. If a cavity is experiencing increased surface losses, which, in turn, means lower Q_0, the cryogenic system must compensate for the increased cryogenic load. Cavities at a specific gradient, with this lower Q_0, would require more power, which increases the operational cost. In some cases, local heating would break the superconducting state, quenching the cavity. Several effects can reduce the performance of SRF cavities. In this section, relevant effects will be discussed, along with any implications they may have on a cavity's performance. Figure 2.4 illustrates the performance degradation caused by the various phenomena.

Multipacting

Multipacting is a resonant electron production phenomenon where electrons pulled from the surface are accelerated by the local electric field impinge on the cavity surface releasing more electrons. If the transit time of the electrons is synchronized to the RF period, an electron production avalanche can occur [28]. The resulting electron avalanche absorbs cavity power and reduces the cavity voltage. Multipacting can be mitigated by careful cavity design and by reducing the secondary emission coefficient at the surface by baking or RF conditioning. RF conditioning typically involves both pulsed and cw conditioning with forward power near and above the level associated with the multipacting barrier.

Thermal Breakdown

Thermal breakdown can occur at defects that are present along the superconducting inner cavity surface. Defects can produce local Joule heating, raising the temperature of the surrounding surface area. Ideally, the heating created can be dissipated into the surrounding Helium bath, but the additional heat will increase R_{BCS}, which, on a local scale, creates more surface losses. Gradual gradient increases will continue temperature growth until the rate of heating surpasses the cooling capabilities. Eventually T_c will be exceeded. As a result, a normal conducting zone will emerge from the formerly superconducting region, and propagate along the inner cavity surface due to the substantial power losses created through the transition. Referring back to Figure 2.4, an example of the transition can be seen by the characteristic Q_0 drop at 6 MV/m. Typically for 1.3 GHz elliptical cavities, superconducting Q_0 values hover around 10^{10}, while normal conducting values decrease to 10^4. The gray curve shown highlights this sudden drop in Q_0.

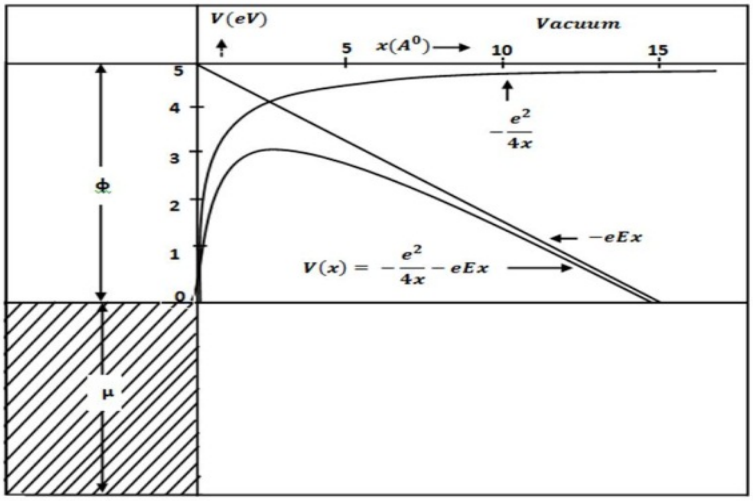

Figure 2.5: Illustration of field emission from a metallic surface. The characteristic triangular potential barrier formed from the presence of an electric field is what allows for a non-zero possibility of electron tunneling. Reproduced from [30] under fair use.

Field Emission

Surface cleanliness is a necessity when aiming to achieve high cavity gradients. If proper cleaning preparations are not made prior to testing, the cavity is likely to experience field emission. Field emission is a quantum mechanical tunneling effect where the strong surface fields interact with dirty surfaces or particulates to pull, and accelerate, electrons out of the contaminates. Particulates with sharp or pointed features, known as emitters, are largely considered as the primary contributor of field emission. The presence of loose electrons in the RF space can jeopardize the accelerating capabilities of the cavity in several ways. Specifically, electrons will be accelerated by the electric fields and either re-deposit into the cavity walls, creating bremsstrahlung X-rays and local heating effects, or be accelerated down the beam axis. Studies have also shown that the presence of hydrocarbons can also degrade the performance of SRF cavities [10]. Although similar, the forming mechanisms behind the two types of field emission differ fundamentally. Furthermore, the differences between the two are not entirely obvious without a deeper understanding of the theory behind field emission. As such, an analytic explanation of field emission, presented by Fowler and Nordheim [29], will be introduced to identify the effect of each contaminant.

Under normal circumstances, electrons will not cross the potential barrier established by a metal material. Typically, the wave function of the electron experiences a significant attenuating effect when outside the potential barrier, essentially removing any likelihood of

electron transmittance. Fowler and Nordheim noted that if the surface potential barrier could be reduced, the electrons would have a non-zero probability of tunneling into the surrounding environment. To achieve this, Fowler and Nordheim proposed that applying a surface electric field could reduce the surface barrier, see Figure 2.5. Analytically, this barrier can be modeled through the relation

$$V(x) = -eEx \tag{2.38}$$

where e is the elementary charge, E is the applied electric field, and x is position. In addition to the potential barrier, the electron must overcome the attractive force produced by the conducting surface. The resulting potential that is produced from this force can be written as an image charge in the form

$$V(x) = -\frac{e^2}{16\pi\epsilon_0 x} \tag{2.39}$$

where ϵ_0 is the permittivity of free space. By combining (2.38) and (2.39), the net potential can be written as

$$V(x) = -eEx - \frac{e^2}{16\pi\epsilon_0 x} \tag{2.40}$$

For the case of a triangular potential well, Fowler and Nordheim were able to obtain the expression

$$j(E) = \frac{A_{FN}E^2}{\phi}\exp\left(-\frac{B_{FN}\phi^{\frac{3}{2}}}{E}\right) \tag{2.41}$$

for the tunneling current density j. Here ϕ is the work function of the metal, and A_{FN} and B_{FN} are constants with values of 1.54x10^6 and 6.83x10^3, respectively. When applying (2.41) to SRF cavities, it was found that the estimated values of the tunneling current was several orders of magnitude below the experimental findings. However, the same exponential dependence was still observed empirically. As such, (2.41) was modified by a scaling factor known as the field enhancement factor, or β_{FN}, to compensate for the discrepancies between the results. The addition of β_{FN} to the current density equation is as follows:

$$j(E) = \frac{A_{FN}E^2}{\phi}\exp\left(-\frac{B_{FN}\phi^{\frac{3}{2}}}{\beta_{FN}E}\right) \tag{2.42}$$

As previously mentioned, the type of contaminate can affect how the field emission origi-

nates. Understanding the difference allows appropriate countermeasures to be formed. Emitters on the RF surface create variations in β_{FN} as they provide a geometric enhancement of the electric field at the location of a protrusion. The exponential dependence of the field enhancement factor can result in strong field emission reactions. On the other hand, hydrocarbon monolayers target the work function aspect of (2.42). Specifically, these hydrocarbon contaminates hold a lower work function than the Niobium surface. Due to the dependence of ϕ in (2.42), the magnitude of the field emission current will escalate depending on the severity of the changes in the work function.

Presently, field emission remains a key phenomenon that limits the operating gradient in SRF cavities globally. Field emission onset can be derived using Q_0 vs E_{acc} plots. Using Equation (2.42) for reference, the field emission current is expected to follow either quadratic behavior for low electric field values or exponential behavior when the electric field is increased. The influx of introduced electrons absorb the cavity fields, adding another outlet for cavity power losses, which is seen through the characteristic drop in Q_0. In ARIEL cavities, field emission onset is routinely seen around 10 MV/m in operation and vertical testing.

2.2 *In-Situ* Plasma Processing

Field emission mitigation is a time- and resource-expensive procedure. While *in-situ*, high-power RF pulsed processing can be used to burn emitters with some success. Under conventional mitigation methods, cryomodule warm-up and disassembly is required before surface treatments such as High Pressure Rinse (HPR) can be applied. The *ex-situ* nature of these practices gives rise to large experimental down times and may not guarantee the removal of persistent contaminates, such as hydrocarbons in the form of C_xH_y or adsorbate gasses. Plasma processing is an *in-situ* cleaning technique that specifically targets these contaminants to improve the work function of the Niobium cavities. Plasma processing technology was first adopted from the semiconductor processing industry, where it has been extensively studied and used to remove organic contaminants [31, 32]. This technique was first extended to the SRF community by SNS to clean their SRF cavities [10, 33]. Now, plasma processing has seen successful on-line applications globally including: the Continuous Electron Beam Accelerator Facility (CEBAF) at Jefferson Lab [34], and the Chinese-Accelerator Driven System (C-ADS) at the Institute of Modern Physics, Chinese Academy of Sciences [35]. This section introduces the plasma processing technique. First, a brief overview of plasma behavior will be provided in Subsection 2.2.1. Subsection 2.2.2. will utilize the concepts shown in

the preceding chapter to describe the working principles of plasma processing.

2.2.1 Plasma Basics

Similar to how a solid transitions to a fluid state when heat is supplied, gasses can be turned into a plasma. The word plasma is designated to a gas that has been, in some capacity, ionized. To provide a more rigorous definition, plasma refers to a gas composed of neutral and charged species that is *quasineutral* in nature, which simultaneously exhibits *collective behavior* [36]. Quasineutrality simply states that the entire plasma holds an equal amount of positive and negative charges thus appearing neutral macroscopically. Locally, the charge distribution will continually change. Unlike a stable gas, the movement of a single charged particle can influence numerous surrounding particles through local accumulations of charge. In particular, these concentrations of charge can induce electric or magnetic fields that will influence the motion of nearby particles using Coulombic forces. Coulombic forces are considered to be long range within a plasma, and their influence can envelop a significant portion of charged particles. Therefore, if external perturbations are applied to a plasma, any changes observed are the collective effect, or behavior, of many particles.

One prominent example of collective behavior within a plasma is its ability to shield out any electric potentials applied to it. Whenever internal electric fields are created in the plasma, charged particles will reconfigure themselves such that the field is shielded. This effect is a direct consequence of the high conductivity produced within plasmas and will produce clouds of charge around the electric field source, polarizing the overall plasma. The length scale of this shielding is known as Debye length, and is given by

$$\lambda_D = \sqrt{\frac{\epsilon_0 k_B T_e}{N_e e^2}} \tag{2.43}$$

where λ_D is the Debye length, T_e is the average plasma temperature, and N_e is the electron density.

When particles in a plasma undergo collective behavior, there will be a given time period of turbulent ion and electron behavior before each particle type can reach an equilibrium state. In particular, electron movement will permit the ions to produce a restoring electric field to force the electrons back into their initial position. Similar to a mass-spring system in simple harmonic motion, the electron will accumulate some inertia on its path back, thus allowing its trajectory to overshoot its preferred location. This cycle will repeat itself, constraining

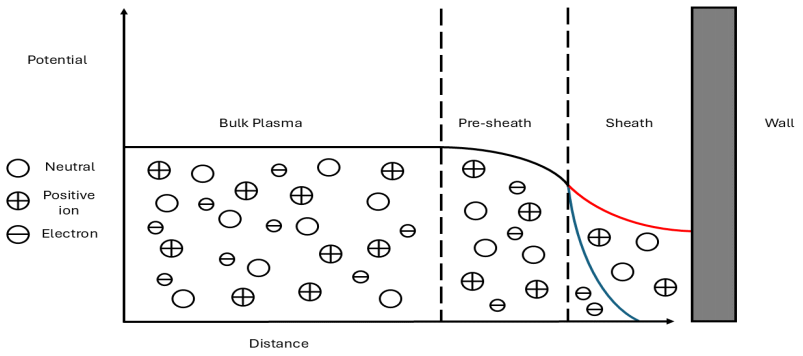

Figure 2.6: Illustration of a plasma sheath. As the plasma approaches the wall boundary, the number of ions continues at a similar rate, shown by the red curve. Electron number, as shown in the blue curve, is held relatively fixed as the plasma aims to maintain the quasineutrality condition. Over time, the wall accumulates more of a negative charge. Inspiration for the image provided by [37].

the electron to oscillate with a frequency known as the plasma frequency until it settles at its equilibrium position. The plasma frequency can analytically be estimated using

$$\omega_p = \sqrt{\frac{N_e}{\epsilon_0 m_e} e^2} \tag{2.44}$$

where m_e is the mass of an electron.

Typically, plasma will be confined in some experimental vacuum environment. The interaction between the plasma and the wall boundary creates a recombination effect with both the ions and electrons. However, the mobility of the species are not equal. Electrons possess thermal velocities higher than ions, therefore leading to a higher loss rate with the wall boundary. As this effect continues, the wall will gather a net negative charge, forcing the plasma to form a positive potential layer several Debye lengths thick across the wall boundary to preserve the quasineutrality condition. This layer is called the plasma sheath and is illustrated in Figure 2.6 along with the pre-sheath, the point at which this boundary begins to affect the bulk of the plasma.

The dielectric constant is used to describe the propagation of electromagnetic waves in a plasma. For high frequency driving signals ($\omega > \omega_p$), the dielectric constant can be written as

$$\epsilon = \epsilon_0 (1 - \frac{\omega_p^2}{\omega_0^2}) \tag{2.45}$$

where ϵ is the plasma dielectric constant, and ω_p is found using (2.44).

2.2.2 Processing

Plasma processing is a room temperature chemical surface restoration technique that is performed within an SRF cavity held under vacuum. First, an inert gas, such as Helium or Argon, is bled into the cavity environment until a cavity pressure in the mTorr range is achieved. From there, a reactive gas, namely Oxygen, is injected into the cavity environment. The gas is then ignited into a plasma by using the cavity fields for a specific operating mode. Each respective gas has a unique interaction with the surface hydrocarbons. The inert gas has a physical bombarding effect on any molecules present along the surface of the cavity. Specifically, ions will experience an accelerating effect from the bias voltage provided by the plasma sheath. The ions are then incident onto the material surface, bombarding any hydrocarbon contaminants present. Chemical chains with binding energies lower than the kinetic energy of the incident ion are cracked into reactive subspecies. Opened bonds are then reformed with the attractive Oxygen molecules present in the plasma, creating volatile byproducts that are then pumped out before they can redeposit back onto the cavity surface. A summary of this effect is shown on the left hand side of Figure 2.7. On the right is an example of this process within a 1.3 GHz Copper cavity using a Helium-Oxygen recipe. Some common formations produced from this process are H_2, H_2O, CO, and CO_2.

The *in-situ* application of plasma processing makes it difficult to directly view the location of the plasma within the cryomodule. However, if plasma ignition is considered as a perturbation to the cavity fields, any changes in the resonant frequencies can be applied into Slater's theorem to estimate the plasma's physical location within an SRF cavity [9]. This modification of Slater's theorem is written as

$$\frac{\Delta\omega}{\omega_0} \approx \frac{1}{2\omega_0^2} \frac{\int_{plasma} \omega_p^2 |\mathbf{E}|^2 dV}{\int_{cavity} |\mathbf{E}|^2 dV} \tag{2.46}$$

where $\Delta\omega$ is the frequency shift of a particular resonant mode. As seen, the magnitude of a resonant mode's shift depends on the driving frequency, along with the strength of the electric field in the cell where the plasma is located. Furthermore, by Equation (2.45), it is known that the frequency shift due to plasma will never decrease. The response of the electric field will be enhanced by the ignition of plasma, creating an upward shift in resonant frequencies. By observing these changes in resonant frequencies, a real-time confirmation of plasma ignition is possible, along with the identification of plasma location within multi-cell

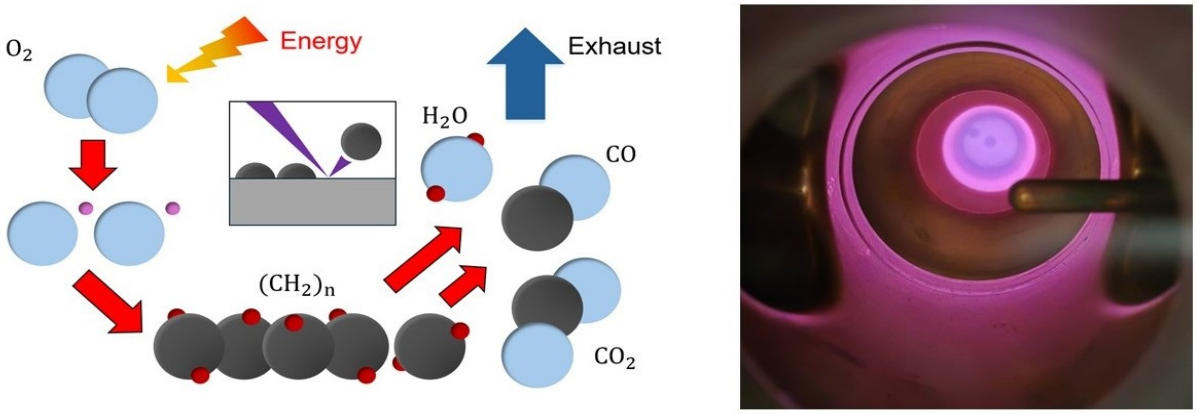

Figure 2.7: Pictured on the left is an overview of the plasma processing reaction that occurs within a cavity. Inspiration for this image provided by [38]. Here, O_2 (blue) is radicalized and made incident onto hydrocarbon chains (gray). Hydrocarbons then form with the reactive Oxygen molecules to form byproducts. On the right is the physical realization of the process shown on the left. This is done using a recipe of Helium and Oxygen within a 5-cell 1.3 GHz Copper cavity.

structures for the various driving modes.

Equation 2.46 can be utilized to extract the plasma's physical location in multi-cell cavities from the frequency shift data. Specifically, the electric field magnitude in each cavity cell will fluctuate depending on the driving mode. Cells with a higher overall electric field magnitude will have a greater likelihood of striking a plasma. Depending on the driving mode, several locations may have similar chances with plasma ignition. As previously mentioned, within an N-cell cavity operating in the fundamental mode, a passband with N modes will be formed. The resulting modes have a field distribution with a K number of peaks, and a K-1 number of zero-crossings. For example, in a 5-cell cavity, the $\frac{3}{5}\pi$ mode will have three equally spaced high electric field peaks, with two locations in which there is no observable field present. However, the relative magnitude of each electric field peak is not guaranteed to be equal. As such, visualization of the field behavior is handled by beadpull plots (see Section 3.2). By directly analyzing field amplitudes as a function of longitudinal distance, frequency shift data can be correlated to cell locations.

Chapter 3

Methodology

Three cavities were subjected to a combination of testing that can be separated into three categories: beadpull, plasma cleaning, and cold tests. In this chapter, the general methodology applied to each test is described.

3.1 Plasma Processing Assembly

The experimental setup used for plasma processing was inspired from [34] and consists of three primary systems. In this assembly, a gas injection system continuously supplies process gasses into the cavity. An RF system is used to excite the electromagnetic fields within the cavity to strike plasma at a mode-dependent location. Byproducts formed in the plasma reaction are pumped out of the cavity. The following subsections will focus on important components of each system, discussing in detail their specific roles during processing. An illustration of the presented systems is given in Figure 3.1, while Figure 3.2 displays the physical plasma processing assembly.

3.1.1 RF System

The RF system used to ignite and maintain the plasma in the bench experiments is indicated by the black and white components in Figure 3.1. On the diagram presented in Figure 3.1, the left-hand side of the cavity holds an input coupler. The input coupler is used to excite the cavity electric fields. The other antenna in the system is located on the opposite end of the cavity and is known as the pick-up probe. A pick-up probe differs from an input coupler in that only a small fraction of the cavity fields are taken through it. Here, it is used to complete the cavity circuit, allowing a network analyzer to measure transmission

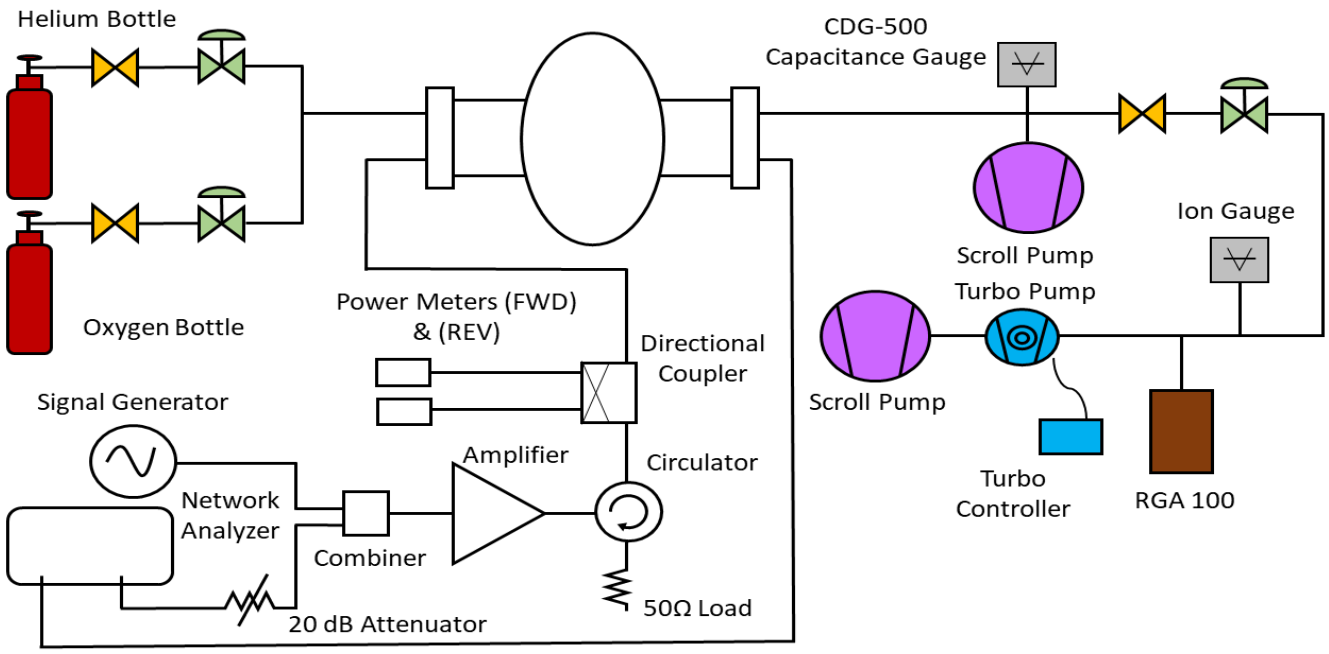

Figure 3.1: Schematic of the plasma processing apparatus.

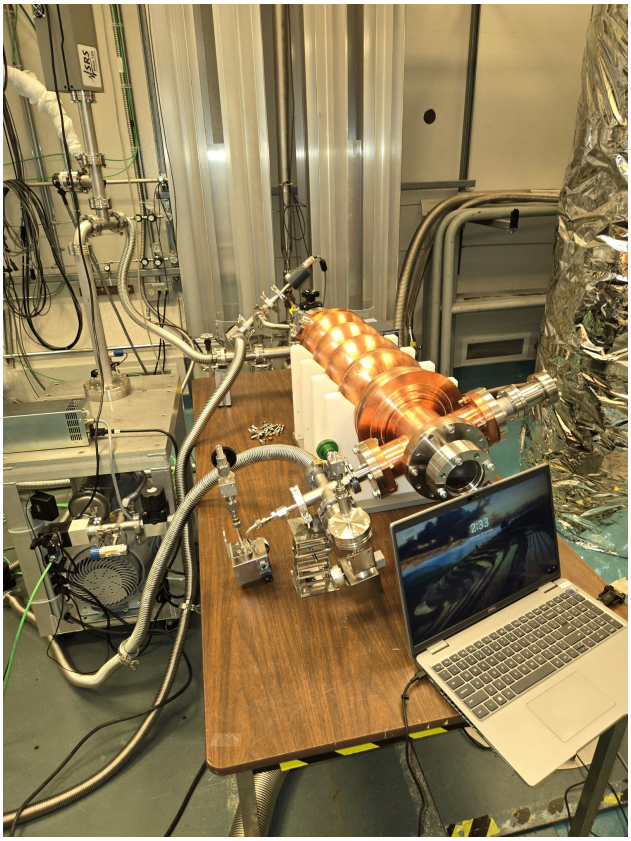

Figure 3.2: The on-bench plasma processing assembly. Here, the 1.3 GHz 5-cell RF cavity is being used to understand how plasma processing can be used in multi-cell cavities.

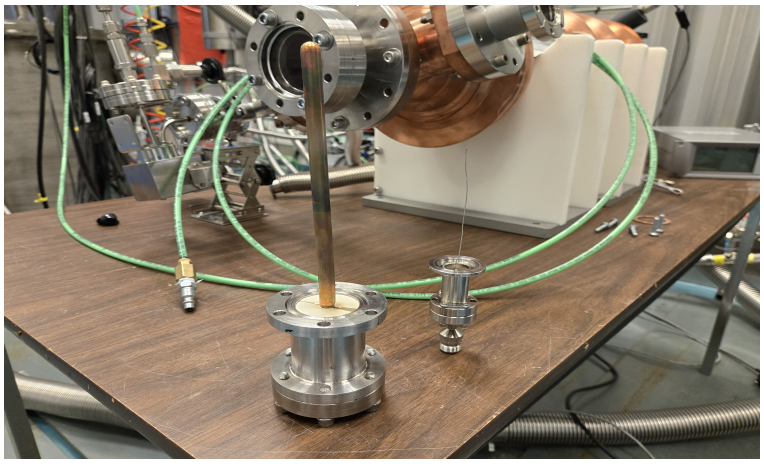

Figure 3.3: Pictured, are the two RF antennas, the input coupler (left) and the pick-up (right), used in a standard plasma processing run. Here, each coupler is connected to a conflat flange that allows for vacuum-sealed connections onto the cavity.

and reflection coefficients. Both antennas described above are shown in Figure 3.3.

To deliver RF power into the cavity, several pieces of equipment are used. First, RF signals of chosen frequency are sourced from a SMB100A Rohde & Schwarz signal generator. The signal is boosted by the amplifier assembly that is placed just after the signal combiner. The amplifier includes a built-in circulator that serves as a protection mechanism against reflected RF signals.

The RF signal passes through a bi-directional coupler that allows for direct measurements of the forward and reverse powers to, or from, the cavity. To obtain an approximate value of the power reaching the plasma, the relation,

$$P_{CAV} = P_{FWD} - P_{REV} \tag{3.1}$$

can be used. Note that each power quantity applied to Equation (3.1) has already experienced attenuation corrections. Here P_{CAV} is the power that the cavity is encountering, P_{FWD} is the forward power to the cavity, and P_{REV} is the power reflected by the cavity.

Resonant frequency responses are monitored using a Rohde & Schwarz ZNB20 Vector Network Analyzer (VNA), see Figure 3.4. VNAs are multi-port RF measurement devices that measure the magnitude and phase of losses or gains between two ports of an RF network. A VNA produces a stimulus RF signal over a specified frequency range. If mismatches are

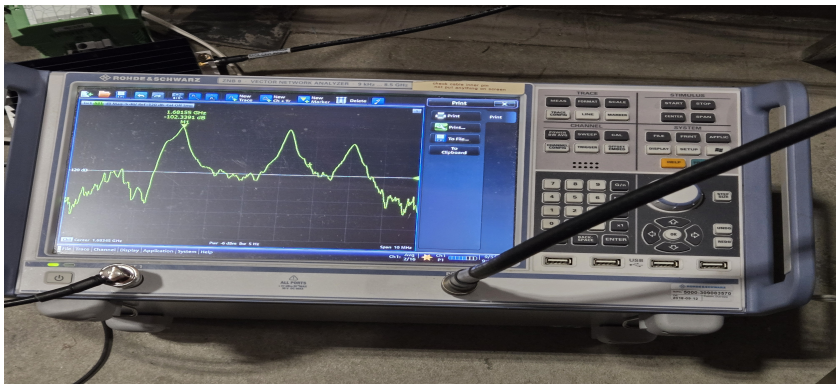

Figure 3.4: A Rohde & Schwarz ZNB20 VNA. Pictured on the screen is the S_{21} signal for HOM's in the ARIEL injector cryomodule.

found within the circuit, some reflection will be produced. VNAs are able to separate incident and reflected signals, which allows for the determination of scattering, or S, parameters. In two-port systems, there are a total of four possible S-parameters, S_{11}, S_{21}, S_{12}, and S_{22}. The subscripts presented are the nomenclature used to distinguish the form of measurement and the port from which the measurement is being taken. S_{11} and S_{22} measurements are reflection measurements for the "1" and "2" ports, respectively. Here, the reflection is a ratio of the reflected signal at a given port to the emitted signal. Conversely, transmission, S_{21} and S_{12}, measurements will compare the signal received at Port 2 from Port 1 and Port 1 from Port 2, respectively.

In the plasma processing assembly, a 2-port VNA is configured to sweep through the observable resonant peaks. The S_{21} responses of the resonant peaks will appear different before and after plasma ignition, as some of the incident signal that was initially transmitted into Port 2 is now reflected due to the plasma. Recalling Equation (2.46), the affected peaks will shift to higher frequencies. Based on the magnitude of the shift characteristics, plasma ignition will be known.

Here, the VNA is in place to act purely as a diagnostic tool. Each particular sweep covers the span of the fundamental passband to observe shift magnitudes resulting from plasma ignition. However, it was noted that during testing, each sweep of the VNA would influence the plasma, temporarily pulling the plasma to follow the sweep. In turn, frequency signals were seen to oscillate between frequencies. As such, a 20 dB attenuator was added to the output signal so that any frequency shifts seen were solely the effect of the ignited plasma.

3.1.2 Vacuum System

The overall vacuum system used in the plasma experiments is comprised of two sub-systems that are responsible for creating fine- (25 Torr - 1 mTorr) and high-vacuum (1 mTorr - 10^{-9} Torr) systems within the experimental setup [39]. The fine-vacuum environment creates and sustains a vacuum within the cavity that can facilitate plasma processing. Cavity pumping was done using a scroll pump, while pressure readouts were handled by a CDG-500 capacitance manometer connected in between the cavity and the scroll pump.

The secondary vacuum system is used to operate sensitive gas diagnostic equipment. The fine-vacuum, or cavity, space creates too much of a gas load to reach high-vacuum conditions efficiently. As such, the gas leaving the cavity is bled into a separate physical space. This is done using a shut-off valve and a leak valve. To achieve high-vacuum conditions, the system is first pumped on using a separate scroll pump. Once the gas load has decreased sufficiently, the scroll pump acts as a backing pump while the space is actively pumped on by a 74 FS TwissTorr turbo pump until a vacuum in the range of 10^{-5} to 10^{-9} Torr is reached. From there, the diagnostic equipment present in this secondary system can begin to run.

There are two important pieces of equipment within the high-vacuum space, a hot-filament ion gauge and an RGA. By design, the RGA is constrained to operate only within high- or ultra-high vacuum regimes. Here, an ion gauge is used to measure the operating pressure to ensure that it is in a safe range for RGA use. The RGA is used to ascertain the byproducts that are formed from the plasma reaction by ionizing gas molecules within the high-vacuum space and separating them based on mass. The particular RGA used here is the SRS RGA 100. With this model, two forms of data visualization can be produced. Molecular partial pressures against mass are taken for fixed intervals of time to display a spectra of mass peaks. The resulting mass spectra is known as a partial pressure versus mass, or PvM, plot. Each sweep of the mass curve provides one data point for each indicated peak. The cumulative array formed through the PvM sweeps can be plotted to display each peak's partial pressure behavior as a function of time. This form of measurement is referred to as the partial pressure versus time, or PvT, plot. As it is assumed that the constituents formed in plasma processing will be evenly distributed upon exit of the cavity, any gas sample taken will be representative of the bulk gas behavior. Keeping this in mind, trends in byproduct formation resulting from plasma ignition can be easily identified using the PvT curve on the RGA. For a successful run of plasma processing, byproducts outlined in Section 2.2.2, are expected to spike with the initial plasma ignition. As plasma continues to run, these elemental quantities

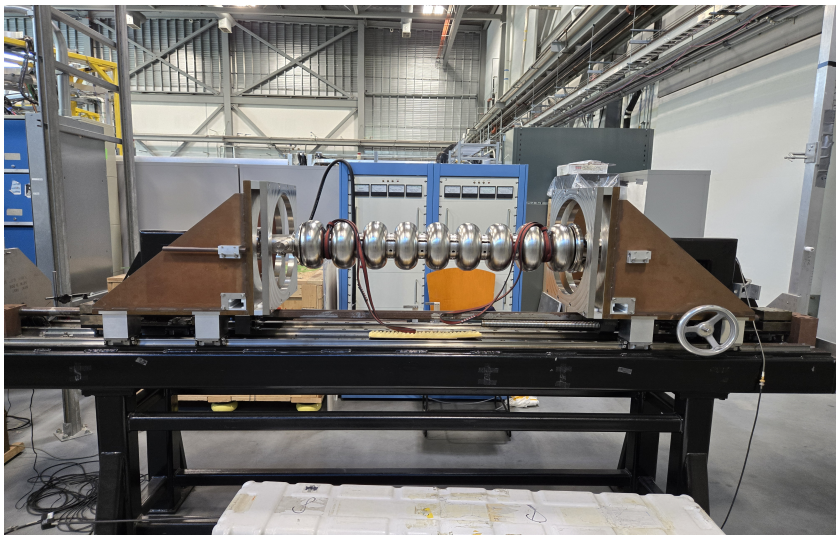

Figure 3.5: The beadpull station used for RF measurements. Attached is the 9-cell 1.3 GHz elliptical cavities used in the plasma processing tests.

will dwindle as they are pumped out of the cavity. Eventually, there will be no indication of byproduct formation, verifying the success of plasma processing.

3.2 Beadpull

Without an optical means of measurement, the plasma location in multi-cell cavities is difficult to determine solely from the resonant frequency responses. However, another prediction scheme can be created using the fact that plasma is influenced primarily by the cavity electric fields. Specifically, by measuring the electric field distribution, the likelihood of plasma ignition can be estimated by identifying the points of largest field amplitude. To obtain the distribution data, a beadpull stand is used. Essentially, a beadpull stand measures the frequency responses that a cavity generates while a metallic bead is pulled through its longitudinal axis. According to Slater's theorem, or a modified version of Equation (2.46), perturbations to the cavity electric fields will elicit a frequency shift that is dependent on the field strength. In this case, the metallic bead will act as the perturbation mechanism, allowing for electric field calculations to be performed based on the observed frequency changes. By pulling the bead through the cavity, the entire electric field distribution for a driving mode can be developed.

The beadpull configuration used for cavity measurements can be seen in Figure 3.5. Not pictured is the hardware utilized in a standard beadpull run. Typically, this will consist

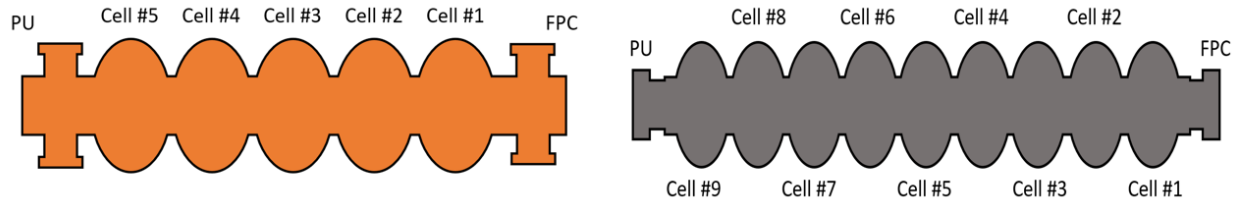

Figure 3.6: Illustrations of the 5-cell RF cavity (left) and 9-cell SRF cavity (right). Here, each cavity is oriented similarly to the beadpull configuration. Cell ordering is based on location in relation to the FPC, which is right to left throughout all provided beadpull plots.

of a VNA, a counterweight pulley, and a step motor. Hardware is managed by a Labview program created to calculate the electric field distributions. Here, the counterweight pulley and the step motor are used to ensure that the bead travels with controlled movement along the center axis of the cavity. The rate of rotation from the step motor, and thus the rate of bead traversal, is handled in conjunction with VNA measurements by the Labview program to collect one beadpull run or sweep. More details can be found in [40], but in short, the VNA is connected to either end of the beadpull bench to measure S_{21} responses in the cavity. The software communicates with the VNA to record mode-specific reference phase signals, frequency, and Q_L prior to beadpull measurements. During data collection, phase signals are taken as a function of bead travel distance. Using the acquired data, electric field calculations are completed in the Labview software to produce a mode distribution across a cavity.

In all measurements, the cavity was oriented so that the FPC end was opposite to the step motor. Subsequent cell references will be made following their position to the FPC, which is located on the right-hand side of each beadpull distribution. Figure 3.6 summarizes this labeling convention illustratively.

The beadpull stand used at TRIUMF serves a dual purpose. Aside from the measurement of RF distributions across the various driving modes, the beadpull stand can permanently alter the shape of each distribution by modifying the length of a particular cell. This is done to uphold the definition of the π-mode. Namely, it is required that the π-mode provides an equal acceleration in each cell throughout the cavity. In other words, this would require that the electric field distributions across each cell must be equal, or "flat"; an example of a flattened cavity is seen in Figure 3.7. Whenever a cavity is not flat, cells will be expanded or contracted between two plates placed at the each iris of a single-cell to progress the field dis-

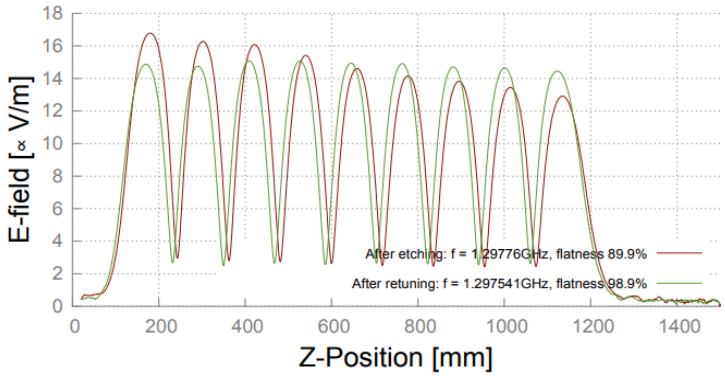

Figure 3.7: An example of a field flattened elliptical cavity. Here, a 9-cell ARIEL SRF cavity was able to reach a flattened π-mode distribution with Buffered Chemical Polishing (BCP) and beadpull tuning [15].

tribution towards a flattened state. Often several cells need to be adjusted, and only when each electric field peak in the π-mode is roughly equal to one another in magnitude will the procedure converge. To know when a field-flattened profile is achieved, a quantification relation defined in [41] can be applied. In analytic form,

$$F.F.[\%] = (1 - \frac{E_{C,max} - E_{C,min}}{\frac{1}{N}\sum E_{C,i}}) \times 100\% \tag{3.2}$$

where $F.F.$ refers to the field flatness as a percentage, and $E_{C,i}$ is the peak electric field amplitude in the i^{th} cell, with the subscripts max and min referring to the largest and smallest fields seen across the N cells.

3.3 Cold Test

SRF cavities are cryogenically tested in a vertical cryostat; the setup used at TRIUMF is shown in Figure 3.8. In this study, vertical tests were conducted on a 1.3 GHz single-cell cavity to qualify the effectiveness of plasma processing at removing field emission. Here, the cold-test assembly and procedure will be discussed.

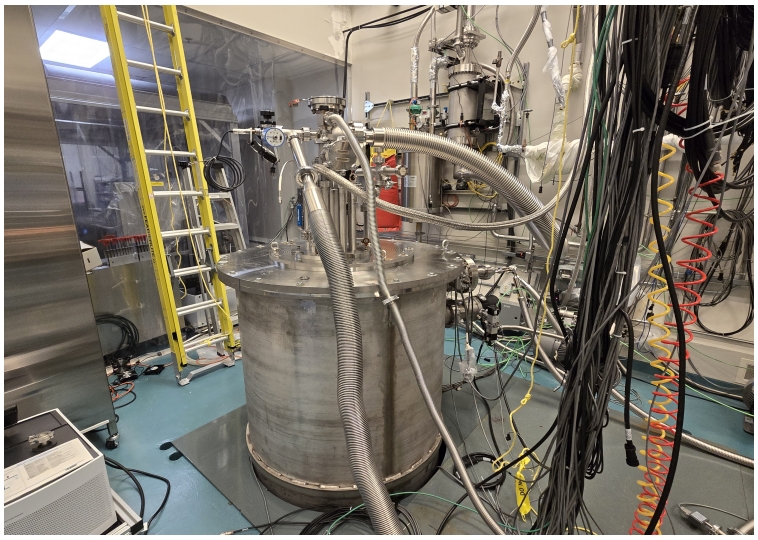

Figure 3.8: The cryostat assembly used for cryogenic testing of SRF cavities. Cavities are lowered into the center of the cryostat, where they will eventually be submerged in LHe.

3.3.1 Cryostat

Cryogenics

To achieve the cryogenic temperatures necessary for cavity testing, a cylindrical vessel known as a cryostat is used. TRIUMF's cryostat includes a vacuum in the space between the cryostat walls that limits convective heat transfer, while a liquid Nitrogen (LN2) cooled shield blocks radiative heat transfer from outside walls [42]. The cavity is suspended vertically in the vacuum space from a removable lid known as the cryoinsert. The cyroinsert is equipped with RF feedthroughs that connect the cavity to external RF sources and copper baffle plates that shield the LHe from radiative heat transfer from the room temperature side of the lid when under vacuum, along with convective heat transfer when in the Helium space. Additional ports on the lid of the cryoinsert create connections to instrumentation. When testing, several types of sensors are placed in areas of interest within the cryostat to relay diagnostic information pertaining to internal parameters, such as pressure, temperature, or LHe levels.

Cavity cool down is done in several steps. First, LN2 is cycled through the cryostat's thermal shield to bring the temperature down to 100K. From there, LHe is used to reach the final testing temperature. A typical test point is 4.2K, the boiling point of LHe at atmospheric pressure. Given the high BCS-resistance at 1.3 GHz, these cavities are typically tested at 2K, a point just below the transition to superfluid Helium. To reach 2K, the LHe must be pumped to $\sim$ 30mbar. Once testing is complete, heaters are used to warm up the cavity

until room temperature is reached.

3.3.2 RF

The performance of an SRF cavity can be characterized using a Q_0 versus E_{acc} curve. An RF circuit is used to excite the cavity at different RF power levels. Using measurements of the forward and reverse powers, along with the cavity voltage, a determination of quality factor and gradient can be made for each set point. To find more details on the LLRF system, refer to [43].

The loaded quality factor can be found by temporarily switching the RF off. Whenever the RF is turned off, the energy will decay following exponential behavior, i.e.

$$U(t) \propto \exp -\frac{\omega_0 t}{Q_L} \tag{3.3}$$

where $U(t)$ here is the time-dependent stored energy. As the stored energy is the square of the cavity voltage, Equation (3.3) can be rewritten as

$$V(t) \propto \exp -\frac{\omega_0 t}{2Q_L}. \tag{3.4}$$

The voltage decay is measured with an oscilloscope and to solve for Q_L, a fit of the same form as Equation (3.4) is applied to find the value of the overall decay constant. As the frequency of the pickup signal is measured simultaneously with the voltage decay, Q_L can be extracted through a simple rearrangement of quantities.

The vertical test system is typically made to be in a critically coupled state ($\beta = 1$) by using a variable coupler. In a critically coupled system, $Q_0 = 2Q_L$, so calculations of Q_0 are thereby straightforward.

To form a Q_0 versus E_{acc} curve, E_{acc} has to be calculated. By utilizing Equation (2.29), and taking into account cable attenuations, the total power dissipated in this system can be written as

$$P_C = P_F - P_R - P_{PU} \tag{3.5}$$

where P_{PU} is the pickup power attenutation corrected from the power meter. If the standard definition of the quality factor, given by Equation (2.24), is to be applied, then the accelerating gradient can be derived by calculating the stored energy, U. Specifically, E_{acc}

is related to the stored energy using the relation

$$U = CE_{acc}^2 \tag{3.6}$$

where C is a proportionality constant. In practice, C is programmed as a selectable constant that is found using finite element solvers, such as COMSOL or CST. A Labview program then takes the aforementioned quantities as input to produce a calibration Q-curve point. As C is a property of the cavity, it remains constant through testing. All subsequent data points will use the same C value, effectively removing the need for repeated decay-time measurements.

Chapter 4

Results

To systematically clean the SRF cavities within ARIEL's cryomodules, several experimental goals must be realized in a testing environment. First, plasma processing must succeed with cleaning the inner surface of a single-cell cavity. Afterwards, plasma movement in multi-cell cavities must be studied until a systematic procedure is developed that cleans each cell within the cavity. The experiments conducted in this study were done to achieve these milestones. A total of three cavities were studied. For its RF simplicity, a 1.3 GHz single-cell elliptical cavity was used to validate and optimize the plasma processing procedure. Plasma movement studies were then conducted using a 1.3 GHz 5-cell Copper RF cavity and a 1.3 GHz 9-cell Niobium SRF cavity. The copper cavity was equipped with ARIEL style end groups while the nine-cell cavity had TESLA style end groups. This chapter focuses on each experiment, discussing the impact of the results towards the eventual on-line implementation of plasma processing.

4.1 Beadpull Measurements

Both multi-cell cavities were attached to the beadpull stand to measure every field profile in their fundamental passband. The beadpull field profiles for the 5-cell can be seen in Figure 4.1, while the 9-cell profiles are in Figure 4.2. In both cases, the first mode was unable to be captured because of poor transmission through the cavity, likely due to poor coupling of the antenna to the mode. Adjustments were made to the beadpull stand in an attempt to improve transmission, but the expected result was unable to be produced. As such, the first mode for each cavity was modeled using COMSOL, a finite element solving software [44]; both plots can be seen in Figure 4.3. The beadpull data of the π-mode is typically used to provide a visual gauge to determine whether cavity tuning is necessary. Typically, a TESLA

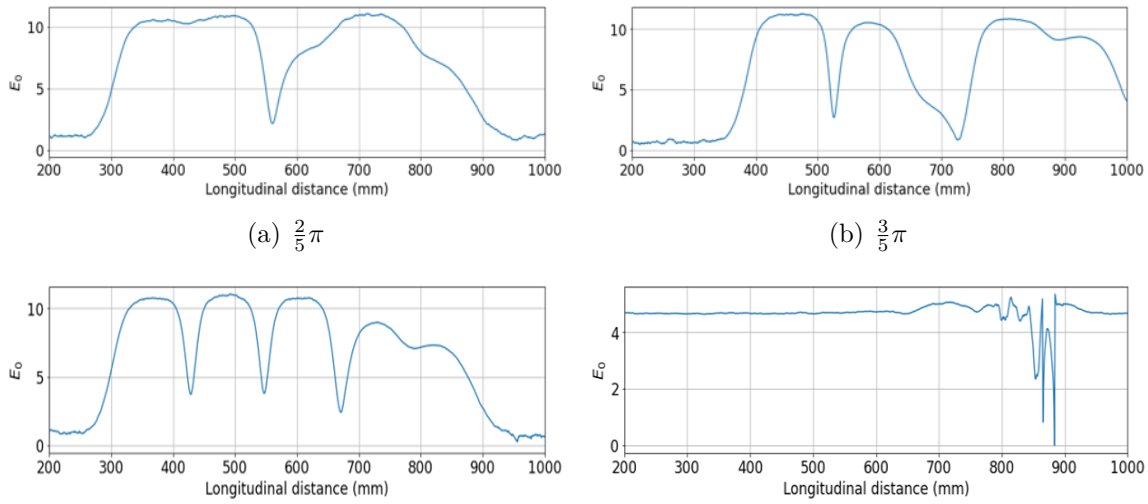

(a) $\frac{2}{5}\pi$ (b) $\frac{3}{5}\pi$

(c) $\frac{4}{5}\pi$ (d) π

Figure 4.1: Electric field distributions across the beam axis within the 1.3 GHz 5-cell ARIEL RF cavity for the various driving modes. Labels correspond to the driving mode of the produced distribution. Here, the left-hand-side of each plot corresponds to the pick-up end of the beadpull stand.

cavity is tuned such that a flatness value greater than 95% is produced in its π-mode. Visually, the magnitude of each peak will be roughly uniform across the passband. The π-mode profile for the TESLA 9-cell shown in Figure 4.2(h) was only 72% flat. Although not close to design specifications, 9-cell tuning was deemed unnecessary. It can be observed that in Figure 4.2(h) the region where the field is the highest is on the pick-up end of the cavity. A gradual downward trend is noted in the field amplitudes towards the coupler end.

In the case of the 5-cell, the last mode in the fundamental passband produced a problematic distribution (Figure 4.1(d)). Unfortunately, noise overshadows the exact curve behavior, making it difficult to determine the field behavior. The source of the noise is still not fully understood, but it persisted until several tuning rounds were applied. The altered field distributions after tuning are seen in Figure 4.4.

After tuning, the $\frac{4}{5}\pi$- and π-modes were the only ones to experience any notable change. Notably, the π-mode had experienced a reduction in noise, now allowing two additional peaks to be resolved. However, the π-mode distribution could not be fully recovered. Specifically,

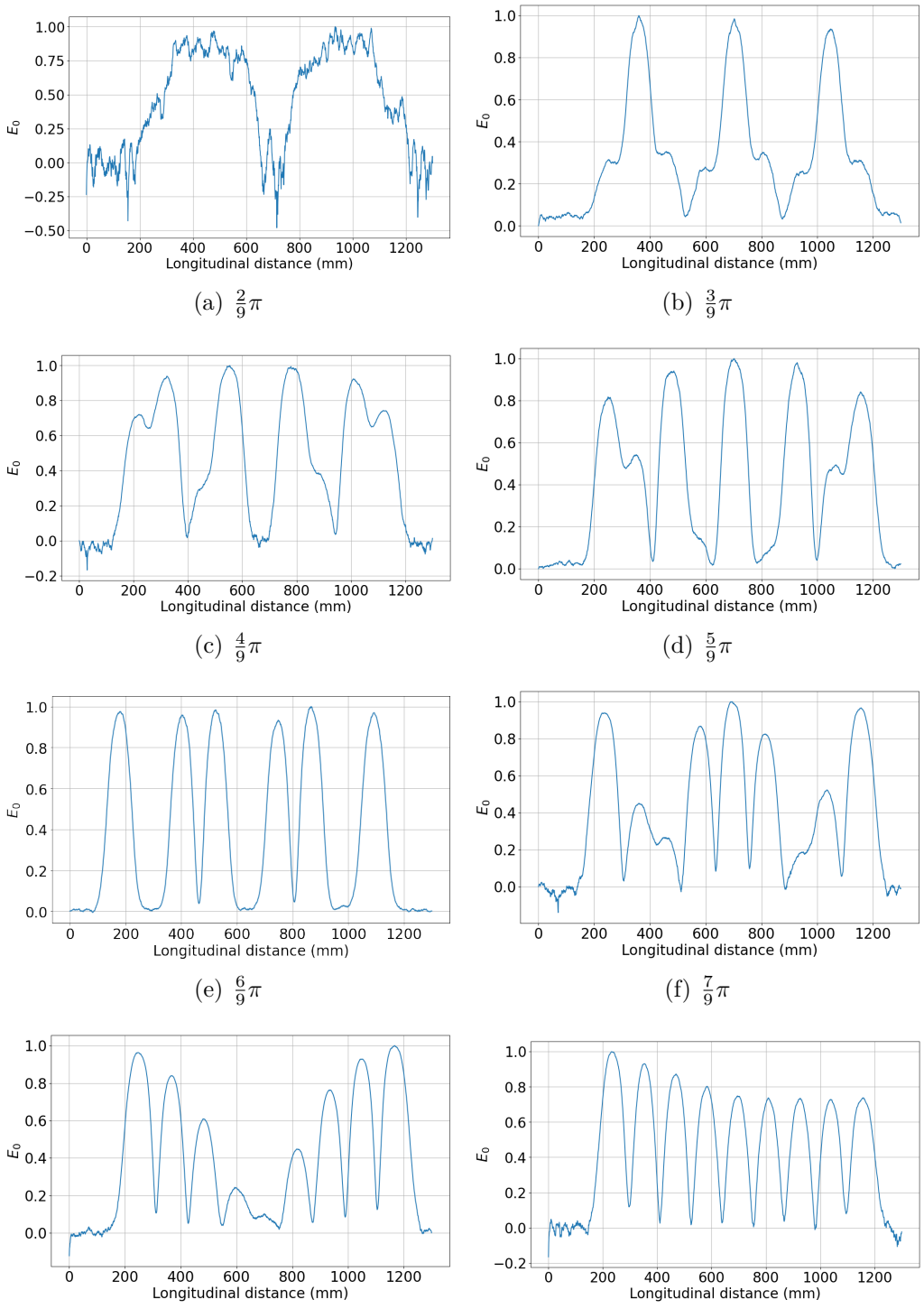

(a) $\frac{2}{9}\pi$ (b) $\frac{3}{9}\pi$

(c) $\frac{4}{9}\pi$ (d) $\frac{5}{9}\pi$

(e) $\frac{6}{9}\pi$ (f) $\frac{7}{9}\pi$

(g) $\frac{8}{9}\pi$ (h) π

Figure 4.2: Longitudinal electric field patterns for the 1.3 GHz 9-cell TESLA SRF cavity. Similar to Figure 4.1. the pick-up end is located at the left-hand-side of the plots.

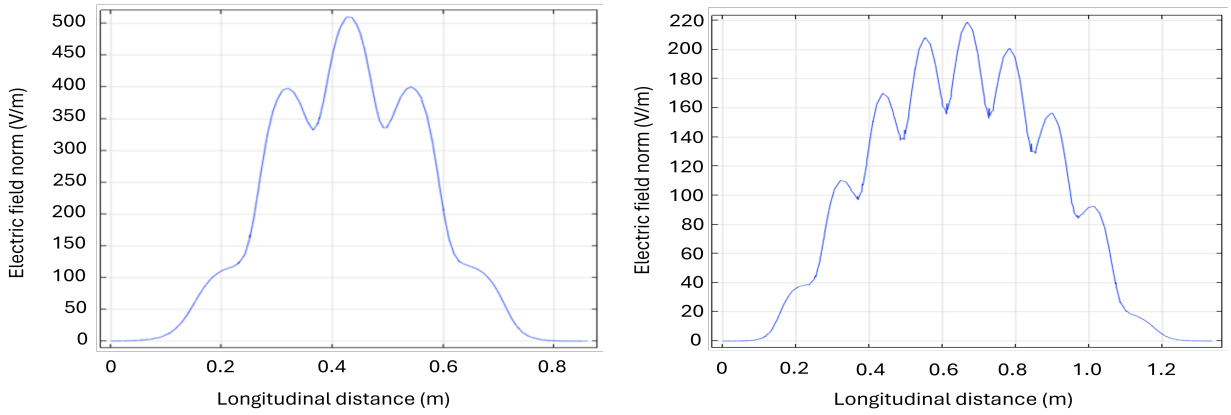

Figure 4.3: COMSOL's recreation of the $\frac{1}{5}\pi$- (left) and the $\frac{1}{9}\pi$-modes for the 1.3 GHz 5-cell ARIEL RF and 1.3 GHz 9-cell TESLA SRF multi-cell cavities.

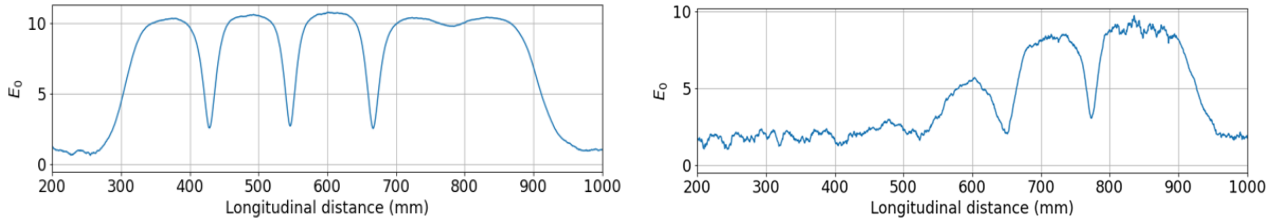

(a) $\frac{4}{5}\pi$ (b) π

Figure 4.4: Beadpull measurements for the 1.3 GHz 5-cell ARIEL RF cavity after several rounds of tuning.

the fields in the two cells closest to the pick-up side of the cavity (200 mm) could not be resolved. In other words, the coupling to the fields in these cells was too weak to achieve a significant field reading. Upon further inspection, it was discovered that there were several cavity fabrication flaws that would explain the poor cavity coupling. Most notably, the radius of each inner cell iris was found to vary significantly across the cavity. Starting from the coupler beam pipe, the iris radii values were measured to be: 48.1 mm, 38.74 mm, 37.09 mm, 36.13 mm, 35.63 mm, and 39.07 mm. The 5-cell was initially designed to test fabrication steps for the ARIEL cavity. In the ARIEL design, the iris radii are fixed at values of 35 mm for the inner half-cells, 48 mm for the coupler beam pipe, and 39 mm for the pick-up beam pipe [15]. Both beam pipe radii seemed to match design expectations well, so the poor coupling experienced could be a direct consequence of the inner cell iris radii deviations. Regardless, the labeling convention $\frac{n}{5}\pi$ cannot be used to describe the modes found in the

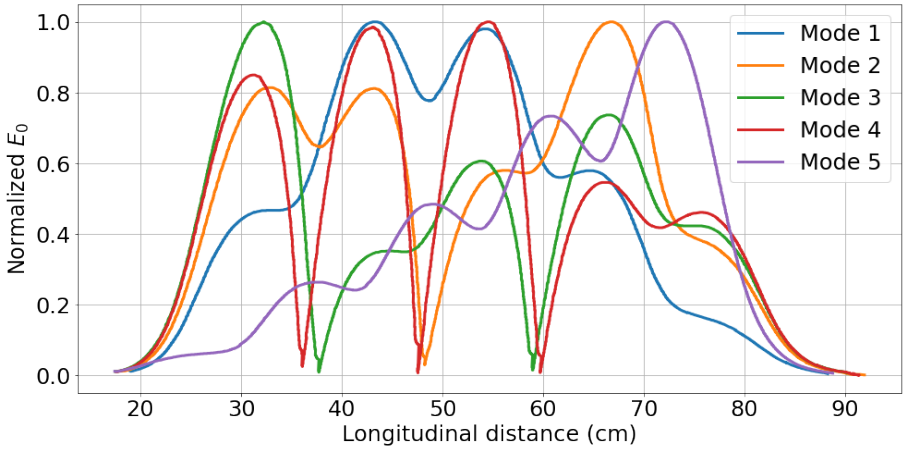

Figure 4.5: Electric field magnitudes for each mode predicted by Poisson SUPERFISH for the 1.3 GHz 5-cell ARIEL RF cavity. Distributions were plotted using Python and found after applying realistic cavity parameters, such as the measured iris dimensions.

fundamental passband. As such, each mode studied in the 5-cell's fundamental passband will be henceforth referred to by the order of its frequency. In other words, the mode with the lowest frequency will be labeled as "Mode 1", and so on.

Once it was determined that the cavity deviated from the design specifications, the 5-cell was remodeled in Poisson SUPERFISH with measured dimensions to verify that the limit of cavity tuning had been achieved. Poisson SUPERFISH is another finite element software that calculates fields within RF cavities [45]. The cavity modes were simulated following cavity parameter adjustments and plotted similarly to the beadpull plots. These distributions are shown in Figure 4.5, indicating good agreement with the beadpull profiles of the actual cavity. The only discrepancy appears to be with the relative magnitude of some peaks. Otherwise, this model was able to accurately replicate the fields within the 5-cell. The SUPERFISH model was then used to help predict the next tuning steps. However, to achieve a roughly flat Mode 5, several substantial adjustments would need to be made, which would not be feasible without damaging the cavity. As such, no field flatness value could be produced for Mode 5 of the 5-cell cavity.

4.2 Plasma processing

Plasma processing using higher-order modes excited from HOM couplers has been proven to recover the performance of SRF cavities *in-situ* [13, 34]. However, TRIUMF's 1.3 GHz

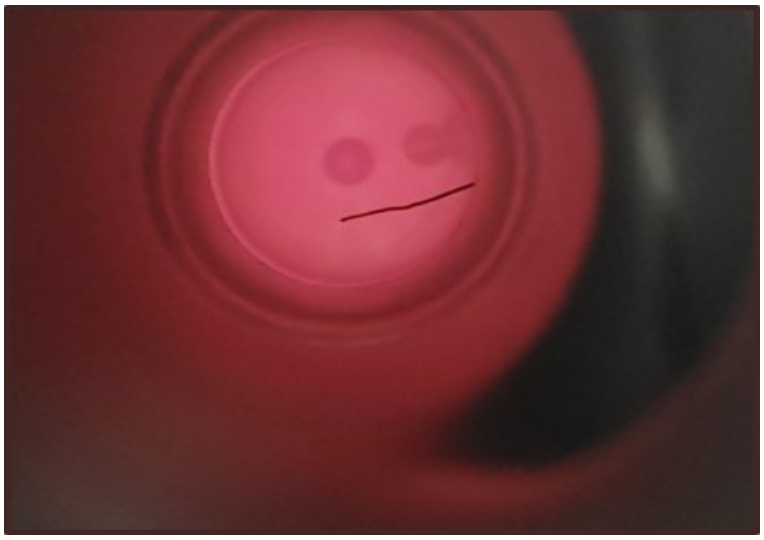

Figure 4.6: An Argon-Oxygen plasma ignited within the 1.3 GHz single-cell cavity.

ARIEL cavities do not contain HOM coupler ports, requiring plasma ignition to be done using FPCs [15]. In addition, HOM's are damped in ARIEL's cryomodules, restricting the available modes to the fundamental and first-dipole passbands [46]. In this research, the fundamental pass band driven from an FPC was used in three cavities. Subsequent sections summarize the findings of each study.

4.2.1 Single-Cell

Sharpie Tests

The initial plasma study conducted on the 1.3 GHz single-cell was done to verify the criteria for igniting a plasma. A combination of 90%-10% Argon gas to Oxygen gas was injected until a cavity pressure of 200 mTorr was reached and a plasma was ignited. Figure 4.6 is an example of the plasma seen through a view port using this recipe.

Initial plasma testing was completed without the RGA in place. In this setup, there was insufficient evidence to determine whether the plasma reaction was working to clean the cavity as intended. Therefore, a demonstration experiment was conducted. In [13], permanent marker points were placed along regions of the inner cavity surface where electric fields were high. Here, a permanent marker is chosen because its ink is composed of hydrocarbons. Through repeated rounds of processing, Giaconne, B., et al. were able to show that these ink markings could be removed. This methodology was applied to the single-cell cavity. Dots of permanent marker ink were placed at several radial locations around the cavity iris.

While pumping on the cavity, no noticeable change was seen in the ink densities. Only when a 90%-10% Ar-O_2 plasma was maintained with a cavity power of 10 W for ten hours was the ink seen to change. These results are presented in Figure 4.7. It can be seen that there are several points in which there is a decrease in ink density. Markings with lower densities are observed to be removed faster than points where the ink is more saturated. Unlike the results found in [13], no point could be fully removed. Furthermore, a majority of the ink in the Giaconne study was processed off in only one hour, rather than our ten. Nonetheless, the contamination created by the permanent marker ink is denser than those adsorbed in an actual cryomodule, so the processing requirements should be less demanding.

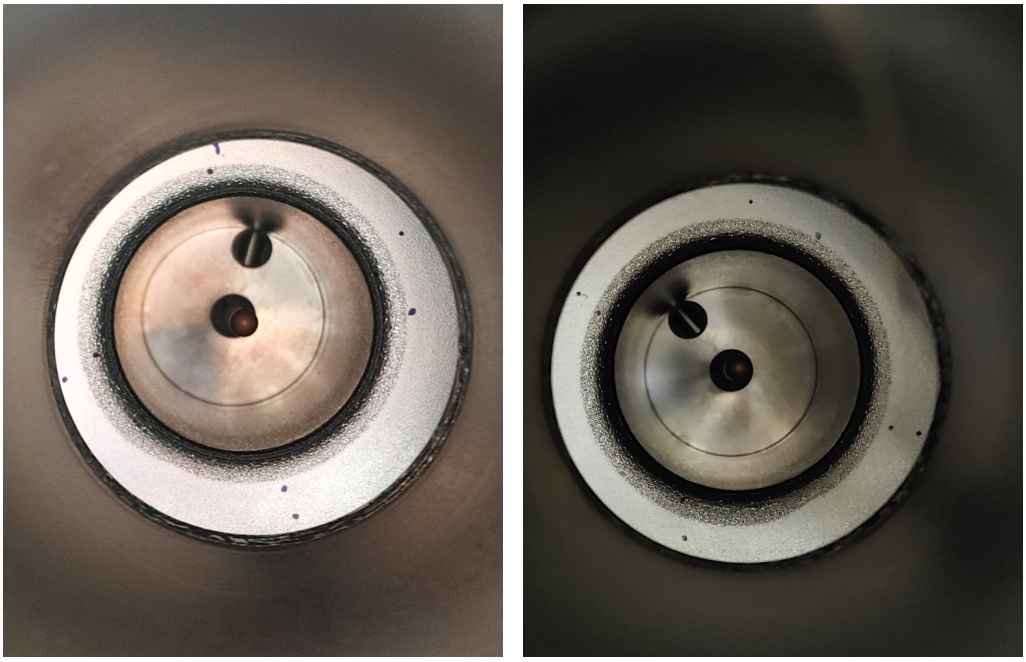

Figure 4.7: The inner iris of the 1.3 GHz single-cell cavity marked with several dots of permanent marker ink (left). The same dots after ten hours of 90%-10% Ar-O_2 processing with 10 W of power going into the cavity (right).

Plasma Processing with the RGA

Following the ink removal tests, UHV equipment was integrated into the plasma processing apparatus. Plasma processing trials were reiterated using a similar gas recipe, namely 90%-10% Ar-O_2 at 200 mTorr. Each processing repetition increased the plasma density in an attempt to promote conditioning efficiency. Specifically, cavity power was increased from the 10 W used in the permanent marker tests to approximately 70 W. Figure 4.8 shows the

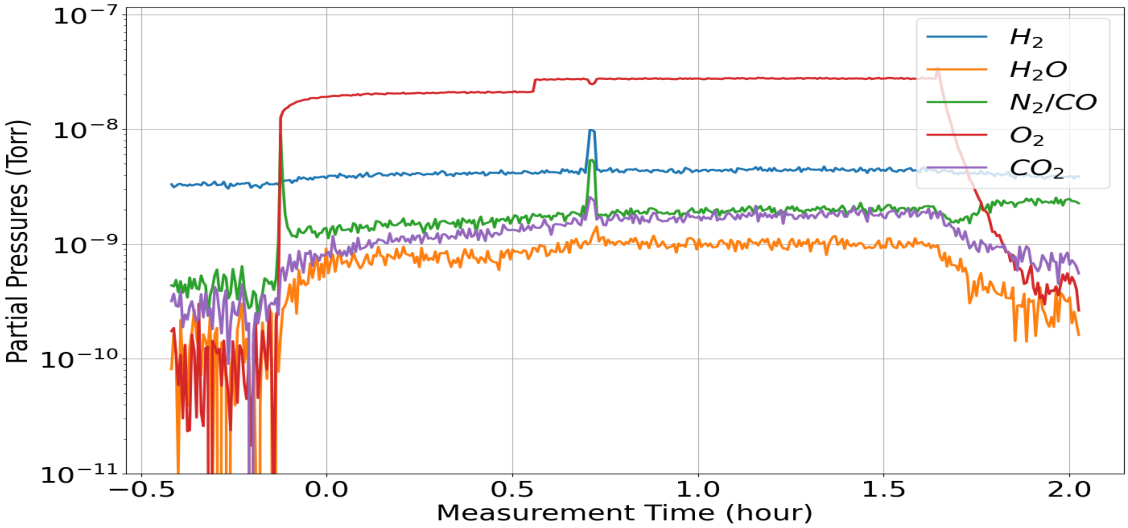

Figure 4.8: The RGA PvT plot measuring the byproduct responses from a 90%-10% Ar-O_2 processing plasma ignited within the 1.3 GHz single-cell cavity. Here, the plasma ignition is set to be at t=0. In addition, a coupler ignition event can be seen to occur at approximately 0.8 hrs.

RGA PvT data collected from one round of processing using this particular plasma recipe. In short, no byproduct responses were seen in any of the performed tests. The only indication of a reaction occurring was the spike seen just past the half-hour mark. Here, the coupler modes were better coupled to the plasma than the cavity modes, and a plasma with a substantial density was ignited along the input coupler, creating a temporary spike in the expected byproducts. This effect was triggered by increases in the input power, and will hereafter be referred to as coupler ignition.

Coupler ignition is problematic for processing because it acts as an upper limit to the available power that can be used to increase the plasma density in the cell. Based on the RGA response, the plasma created in the cell had too low a density to facilitate processing reactions. As such, several recipes were attempted that altered the Oxygen levels in the plasma, the total cavity pressure, or both. Each successive plasma trial produced trends similar to those seen in Figure 4.8.

After private communications with JLab's Tom Powers, the inert process gas was changed to Helium. The testing using Helium as the process gas was a success, though it is not fully understood which elemental property was directly responsible for the change in results. Jonkers, et al. have reported that at atmospheric conditions, Helium's higher excitation po-

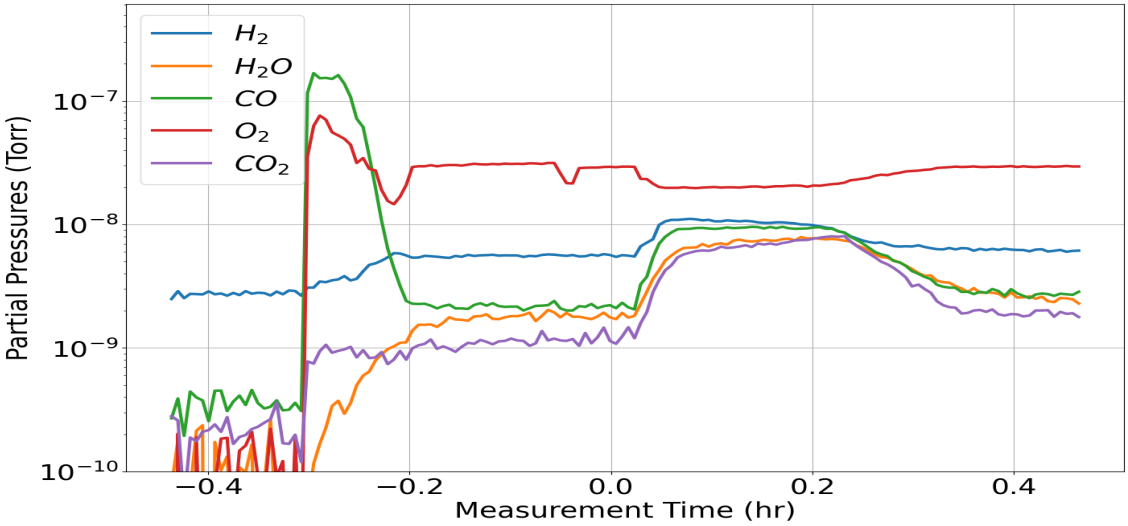

Figure 4.9: The RGA PvT plot measuring the byproduct responses from a 95%-5% He-O_2 processing plasma ignited within the 1.3 GHz single-cell cavity. Byproduct formations are seen to increase shortly after plasma ignition at t=0.

tential of its first excited state and lower overall mass results in a higher electron temperature plasma [47]. If this condition still holds true in our plasma environment, the higher electron temperature could mean that Helium is more capable at facilitating chemical reactions because it has better heat transfer between electrons and heavy ions compared to a similar Argon plasma. Figure 4.9 shows the PvT data measured by the RGA for a 95%-5% He-O_2 cleaning plasma at 80 mTorr. Immediately, the trends exhibited follow expectations. Sharp increases in common byproducts formed in the processing reaction, like H_2O, CO, and CO_2, can be seen at plasma ignition. In addition, the partial pressure of the reactionary process gas, Oxygen, is seen to diminish at a rate similar to the increase in the other byproducts. While processing continues, saturation was observed in the partial pressures. This is the point at which the processing is at a maximum within the cavity. As processing continues, the partial pressures of each byproduct begins to decrease until the background signal overshadows the reaction's behavior. Overall, removal of contaminants within the single-cell cavity took approximately 30 minutes at a power of 100 W using this particular plasma recipe.

Recipe Comparisons

Several conditioning trials were conducted that adjusted parameters to characterize plasma efficiency.

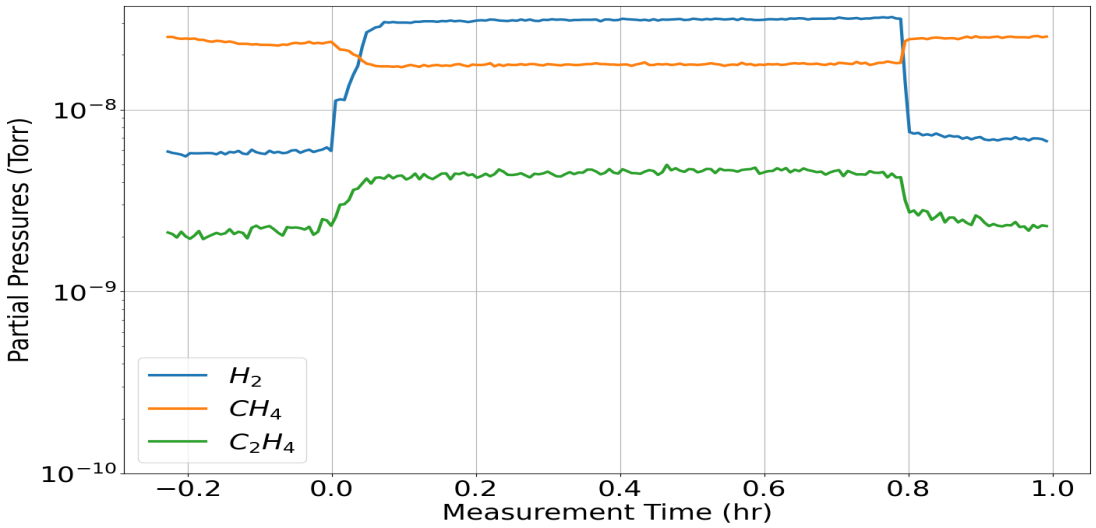

Figure 4.10: The RGA PvT plot measuring the byproduct responses from a 95%-5% He-CH_4 processing plasma ignited within the 1.3 GHz single-cell cavity. Byproduct formations are seen to increase shortly after plasma ignition at t=0.

To normalize the processing comparisons, prior to each processing run, artificial contamination was applied using a Helium-Methane plasma. The idea of Methane pollution was first introduced by JLab [48]. Fundamentally, the Helium-Methane and Helium-Oxygen recipes follow similar cracking principles. Specifically, Helium is used to split CH_4 into its Carbon and Hydrogen constituents, which will deposit onto the cavity's surface. A typical RGA PvT measurement for the contaminating plasma is seen in Figure 4.10. At plasma ignition, constituents like H_2 are seen to spike. Simultaneously, Methane is consumed in the splitting process, which is why it is seen to drop until plasma is extinguished. Interestingly, molecules of mass 28 were seen on the RGA and observed to follow the H_2 behavior. We suspect that this molecule is Ethylene (C_2H_4). During contamination, it appears that particles split in the plasma environment can reform into longer hydrocarbon chains before they are pumped out of the system. Ethylene was the only unexpected hydrocarbon configuration measured.

Several contamination recipes were tested, and it was found that a gas recipe of 95% Helium to 5% Methane at 80 mTorr created the largest contamination reactions. As such, following each processing round, a contaminating plasma using this recipe was maintained for 90 minutes.

Each of the processing recipes tested had their byproduct responses compared to observe

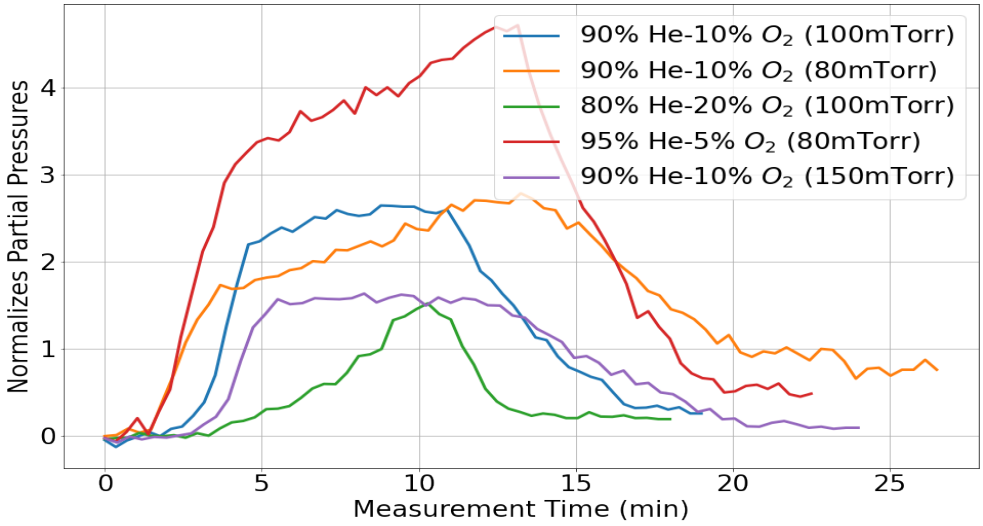

Figure 4.11: A comparison of CO_2 abundances that are removed from the cavity during processing for the tested processing recipes.

which recipe could process most effectively. Direct comparisons were not possible due to differences in the flow rates between recipes. As such, alternative methods of recipe comparison were attempted. Byproduct curves resulting from plasma ignition were normalized by their partial pressure values prior to plasma ignition and plotted against one another. A CO_2 abundance comparison between the various recipes using this normalization can be seen in Figure 4.11. Recipes that elicit strong initial CO_2 responses are seen to also extend the processing period. This behavior is most prominently seen with the 80mTorr 95%-5% He-O_2 (red) and 80mTorr 90%-10% He-O_2 (orange) curves in Figure 4.11.

The trends produced seem to indicate that the choice of gas composition has an inherent effect on the efficacy of plasma with removing hydrocarbons. Recipes with a lower overall cavity pressure are seen to process CO_2 out of the cavity in greater abundances, displaying higher removal rates for extended reaction durations, comparatively. Furthermore, recipes with a higher percentage of Oxygen unanimously perform poorer than recipes that use less Oxygen. This effect is seen in several instances. For example, between the red and orange curves in Figure 4.11. These recipes are the closest in composition, only deviating by 5% in their respective Oxygen ratios, but the red curve has a higher removal rate for a similar processing period. Although both parameters can influence hydrocarbon removal, the PvT data suggests that plasma processing is more dependent on Oxygen quantities present compared to the gas pressure.

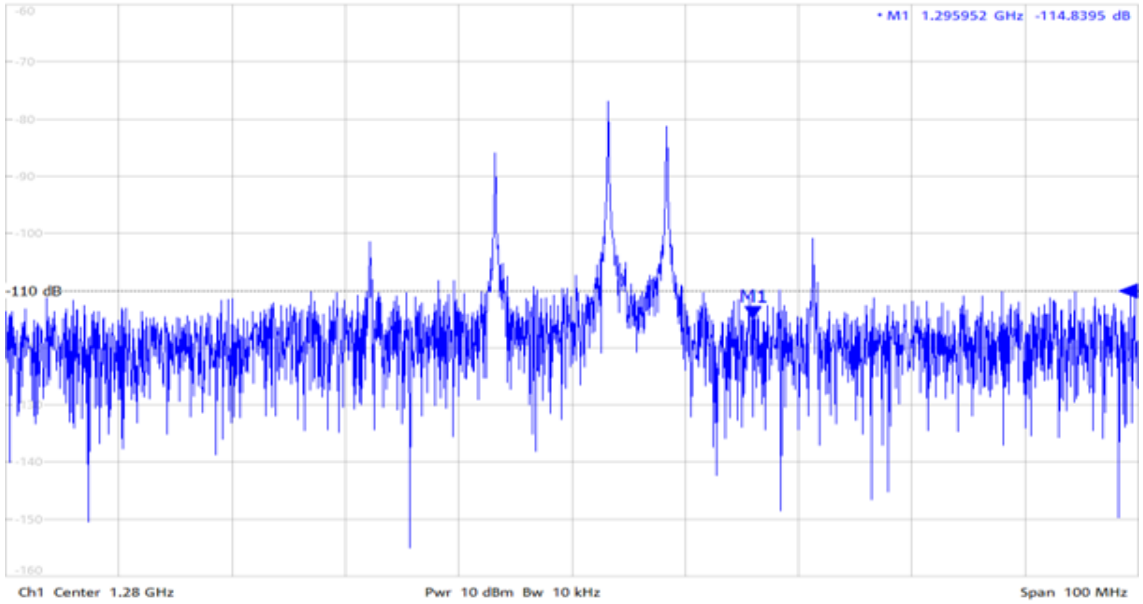

Figure 4.12: S_{21} measurement of the 5-cell's fundamental bandpass using the VNA.

The data collected in this experiment has shown that in general, the combination of low cavity pressure and low Oxygen ratios yielded the greatest byproduct responses. Currently, we cannot conclude that the recipes presented are optimized for on-line application. Additional exploration into recipes with cavity pressures lower than the chosen threshold of 80 mTorr or the Oxygen ratio of 5% is needed to fully understand the limit of each parameter. During testing, high residual vacuums in the cavity space and the rough flow control with manual valves made any subsequent recipe adjustments difficult. Implementation of mass flow controllers would allow for fine gas adjustments, while more rigorous assembly of the plasma apparatus would reduce the residual vacuum.

4.2.2 5-Cell

Network Analyzer Measurements

Although the 1.3 GHz 5-cell ARIEL cavity exhibited poor electric field distributions in the beadpull measurements, processing studies can still provide useful information on the nature of plasma ignition within the various modes in the on-line cavities. Before subjecting the cavity to plasma processing experiments, the VNA was used to collect S_{11} and S_{21} data for every mode within the fundamental passband. The transmission signal for the entire first passband can be seen in Figure 4.12. Observing the passband, it was noted that the first and last resonant peaks, which correspond to Mode 1 and Mode 5, were transmitting

significantly lower than the middle three peaks. Recalling the beadpull distributions, both of these modes were seen to have weak coupling, even with tuning, so this result is not surprising. Furthermore, the coupling of the input coupler to each mode was measured using Smith charts. These results are summarized in Table 4.1. Table 4.1 initially presents the coupling using Standing Wave Ratio (SWR) values. SWR describes the RF mismatch in a waveguide and is defined as the ratio of the maximum and minimum amplitudes in a standing wave. For undercoupled RF systems, SWR can be related to the coupling constant, β, by: SWR $= \frac{1}{\beta}$. Using this relation, every mode was found to be undercoupled. Here, Mode 5 was found to be the closest to a critically coupled system, while Mode 1 was the most undercoupled, comparatively. Critically coupled assemblies have already been shown to successfully process off hydrocarbons (Section 4.2.1). However, when on-line application is considered, critical coupling would be difficult to attain. Specifically, each ARIEL SRF cavity is designed to maintain a Q_{ext} value of 3×10^6. While the cavity is at 2K, the cryomodule is set to operate in an overcoupled state due to the large Q_0 (1×10^{10}) [49]. To apply plasma processing, the cavity must be warmed-up to room temperature, which drops Q_0 to approximately 1×10^4. At this temperature, the cryomodule assembly becomes undercoupled. Therefore, understanding plasma ignition behavior for undercoupled systems will better prepare the eventual on-line implementation.

Table 4.1: VNA measurements of the 5-cell's fundamental passband.

Mode	Coupled State	SWR	β
1	Undercoupled	12.79	0.078
2	Undercoupled	11.77	0.085
3	Undercoupled	10.82	0.092
4	Undercoupled	8.11	0.123
5	Undercoupled	4.15	0.241

Plasma Processing

Processing was conducted using both Argon and Helium recipes. In each of the tests performed, the location of the plasma was visually confirmed through an optical viewport. The optical window was attached on the longitudinal beam port closest to the FPC. It should be noted that since only one viewport was used, the plasma closest to the window would effectively block any visual indication plasma ignited further downstream. In turn, this made it

difficult to determine the exact characteristics of the plasma other than its nearest location.

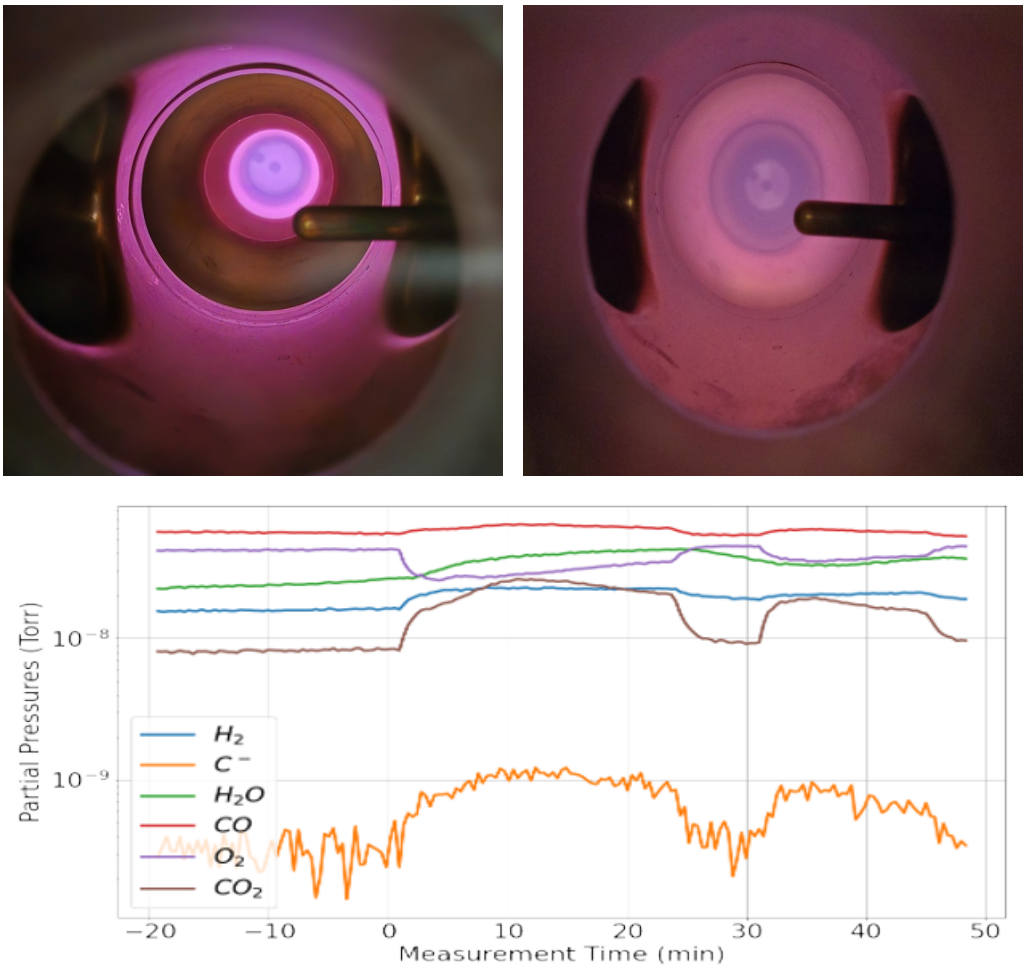

Figure 4.13: He-O_2 plasma ignitions within the 5-cell using Mode 4 (upper left) and Mode 5 (upper right) of the fundamental passband. Plasma locations are seen to ignite in different locations depending on the mode. The RGA PvT scan corresponding to the processing with these two modes is seen below the two plasma images.

Helium ignitions in the 5-cell were conducted first. Each of the frequencies corresponding to the five modes in the fundamental passband were used to drive the cavity fields. Of the five modes, Modes 4 and 5 were successful in creating fields capable of igniting a plasma within the 5-cell. Furthermore, both of the plasmas produced were dense enough to produce RGA byproduct responses. These plasma ignitions were performed consecutively, and are visually summarized in Figure 4.13. We can see that in the upper left and right images in Figure 4.13, bright plasmas are formed in cells 3 and 1. However, when driving the cavity using

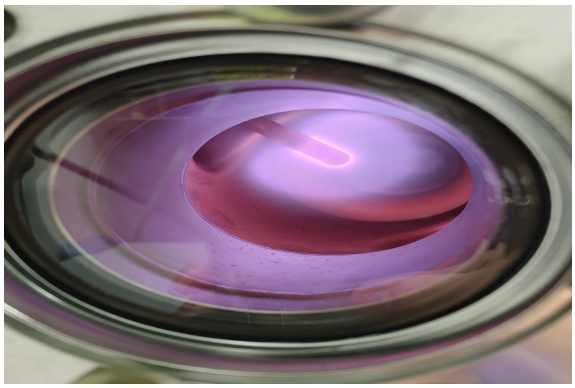

Figure 4.14: Displayed is an Argon-based coupler ignition within the 5-cell. Here the coupler was ignited using Mode 3 and can be identified by the bright purple hue around the antenna tip.

Mode 5, the plasma seen in cell 1 could be the initial ignition location, or the diffusion from a plasma located in cell 2. It is likely to be the former. Recalling the beadpull distributions for these modes, the largest electric field amplitudes are observed around the 3rd and 1st cells for Modes 4 and Modes 5, respectively. Therefore, the experimental observations were consistent with the beadpull predictions when plasma was achievable.

After Helium testing, Argon processing was opted for as it displayed lower ignition thresholds in the single-cell testing. In short, Argon plasma ignition was confirmed in all fundamental passband modes, except for Mode 1. However, none could initiate any byproduct response from the RGA. Similar ignition locations were noted when reattempting ignitions with Modes 4 and 5. Additionally, Modes 2 and 3 created plasmas within cells 4 and 5, both of which were also consistent with their beadpull distributions. It is therefore safe to assume that the first mode would ignite a plasma at the point of highest electric field magnitude. For Mode 1, this would be suspected to occur in the middle of the cavity, likely within the third cell.

Ultimately, the coupling in the earlier modes did pose problems for plasma ignition, making it difficult to observe how mode shifts will influence processing parameters. In addition, coupler ignitions would often occur seemingly unpredictably, limiting the overall power available for plasma density modifications. Before on-line testing can be considered, coupler ignitions must be better understood to form necessary preventative measures, as they have been shown to damage equipment and sputter coupler material onto the cavity [50].

Coupler Ignition Studies

Coupler ignitions were studied systematically within the 5-cell in an attempt to predict their occurrences. During testing, coupler ignitions were identified either visually or by drops in the VNA transmission signals. It was noticed that coupler ignitions, or breakdowns, would occur at various thresholds dependent on the gas recipe. One example is seen in Figure 4.14. Coupler ignitions were induced for the five modes as a function of gas pressure. The results for both Argon and Helium are given in Figure 4.15. In either case, the threshold for coupler ignition is lower at higher cavity pressures. This behavior is more easily seen in the Argon case, where most modes are seen to breakdown around 60 W when cavity pressures are past 300 mTorr. However, the most peculiar behavior is found with Mode 5. Mode 5 is seen to ignite the coupler much lower compared to the other modes.

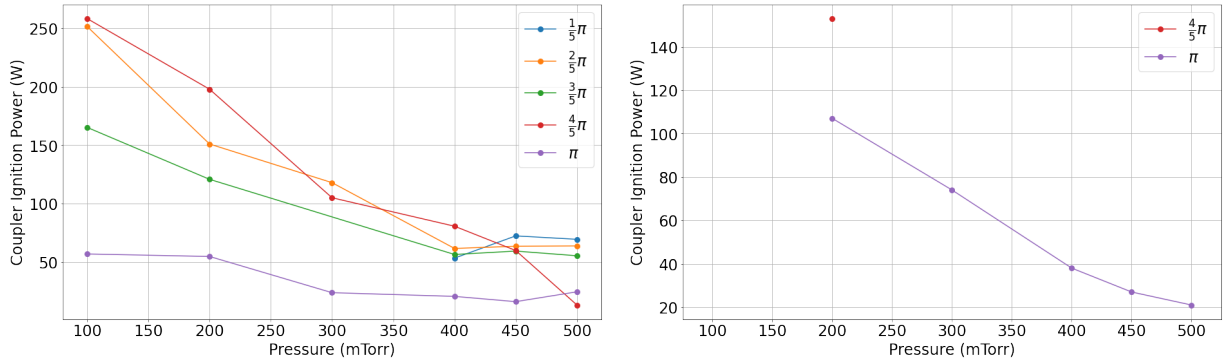

(a) Argon coupler ignitions.

(b) Helium coupler ignitions.

Figure 4.15: Coupler ignitions for the various modes as a function of cavity pressure. The left-hand image is for Argon testing, while the right image is for Helium. Helium coupler ignitions were not seen as frequently compared to Argon testing, only consistently igniting in Mode 5.

Coupler ignition was seen across almost all tested modes for Argon. Initially, it appears that Argon tends to exhibit behavior that supports coupler ignition. However, it is likely that the powers required to ignite the coupler using Helium were never reached. Previously, Helium was seen to need more power to initially transition into a plasma compared to Argon. As powers in the hundreds of Watts were reached for the Argon case, it is likely coupler ignition will not be a problem in subsequent Helium testing, unless a high cavity pressure is used.

Coupler ignition is currently understood to occur when coupler modes become more fa-

vorable to ignite a plasma than the cavity modes. In most cases, this effect is seen after plasma ignition is already achieved. Therefore, plasma ignition through power adjustments contributes to the likelihood of coupler breakdown. Specifically, driving at a cavity resonance allows for efficient power transfer to the cavity fields. Plasma ignition will shift the resonant peak to higher frequencies according to Equation (2.46), pushing the initial drive signal further off-resonance. Off-resonance excitation is less efficient than on-resonance excitation, requiring more RF power to reach equivalent field amplitudes. Ultimately, the process repeats itself. Power increases eventually result in a lower power transfer efficiency, which requires more power to promote the plasma's density. Eventually, the large reflected signal produced from this process would decouple from the cavity modes, and instead tend to the coupler modes, creating a plasma discharge around the FPC. To counteract this, iterations of plasma processing have adjusted the driving frequency following plasma ignition, effectively chasing the resonance to reduce decreases in mode excitation efficiency [9]. To mitigate the possibility of coupler breakdown, this approach should be considered for future multi-cell testing.

4.2.3 9-Cell

The 5-cell cavity was found to be unable to consistently ignite all modes in the fundamental passband. Furthermore, no additional ARIEL cavities were available to continue multi-modal plasma testing. As such, a 1.3 GHz TESLA 9-cell SRF cavity was opted for. The TESLA 9-cell has already been shown to have reasonable RF distributions in its fundamental passband (see Section 4.1.), so the cavity was chosen to provide experience with plasma ignition and movement within 9-cell 1.3 GHz cavities. Although the ARIEL cavity design was originally derived from the TESLA design, there are several differences between the two that require adjustments in the experimental assembly and procedure. An example is that the TESLA cavity only has two ports available for vacuum or RF connections [14], compared to the ARIEL cavity's six. In short, this design choice makes the installation of an optical viewport impractical. Previously with 5-cell plasma testing, the location of the plasma was visually confirmed through the optical viewport. Knowing the plasma location is necessary to develop a cleaning sequence in multi-cell cavities. As such, in this section, a model is introduced that utilizes field concentrations in the TESLA 9-cell cavity to estimate the plasma's location through S_{21} responses.

In the proposed model, plasma location estimation is done using two sets of data. First, it is known that the location of the plasma within the 9-cell cavity is dependent on the

concentration of fields in a particular cell. Cells with higher electric fields are more likely to excite and sustain a plasma. As such, the first set of data this model utilizes is the stored energy data, which is extracted for each cell from the beadpull distributions shown in Figure 4.2 in Section 4.1. Here, the approximate cell positions were estimated using the definition of the π-mode. Specifically, the π-mode is configured to produce similar electric field amplitudes across each of the nine cavity cells. By observing the longitudinal position of each peak, cell locations will be known and used to extract electric field data from all of the beadpull field profiles; collecting all of the data into one table will form a 9×9 electric field matrix, E_{mn}. Electric field measurements are converted to stored energies by squaring each value, and normalized such that each column sums to unity. The resulting matrix, U_{mn} is seen in Table 4.2.

Table 4.2: The normalized stored energies within each cell of the 1.3 GHz TESLA 9-cell SRF cavity as a function of driving mode. Note that the first mode is not presented as it could not be resolved in the beadpull measurements.

	$\frac{2}{9}\pi$	$\frac{3}{9}\pi$	$\frac{4}{9}\pi$	$\frac{5}{9}\pi$	$\frac{6}{9}\pi$	$\frac{7}{9}\pi$	$\frac{8}{9}\pi$	π
Cell 1	0.0639	0.0319	0.0887	0.1519	0.1095	0.1848	0.2040	0.0943
Cell 2	0.1568	0.2538	0.1768	0.0467	0.1137	0.0651	0.1779	0.0921
Cell 3	0.1543	0.0211	0.0196	0.2042	0.1100	0.0137	0.1263	0.0939
Cell 4	0.1114	0.0390	0.2001	0.0014	0.1083	0.1403	0.0518	0.0944
Cell 5	0.0187	0.2830	0.0066	0.2128	0.1136	0.1924	0.0082	0.0958
Cell 6	0.1399	0.0237	0.1872	0.0050	0.1101	0.1530	0.0190	0.1086
Cell 7	0.1629	0.0395	0.0446	0.1847	0.1088	0.0243	0.0813	0.1245
Cell 8	0.1453	0.2835	0.1504	0.0640	0.1136	0.0514	0.1444	0.1392
Cell 9	0.0469	0.0246	0.1260	0.1293	0.1123	0.1750	0.1871	0.1572

The second set of data that this model uses consists of resonant mode frequency shifts. When a plasma is ignited within a cavity, the plasma acts as a perturbation, which shifts the resonant modes to higher frequencies, according to Slater's theorem. Figure 4.16 shows how a plasma ignited with the $\frac{1}{9}\pi$-mode can alter peak frequencies throughout the passband. Using the VNA, peak frequencies are measured by placing a marker over the resonance. By comparing the frequencies of all nine resonant modes in the passband before and after plasma

ignition, the shift of each peak can be directly calculated as the difference between the two quantities. Several driving powers were attempted for each driving mode, and the resulting measurements are summarized in Table 4.3. The columns are organized according to a given mode, while the rows distinguish the cavity power used to excite the plasma. The complete tabulation of the frequency measurements is provided in Appendix A.

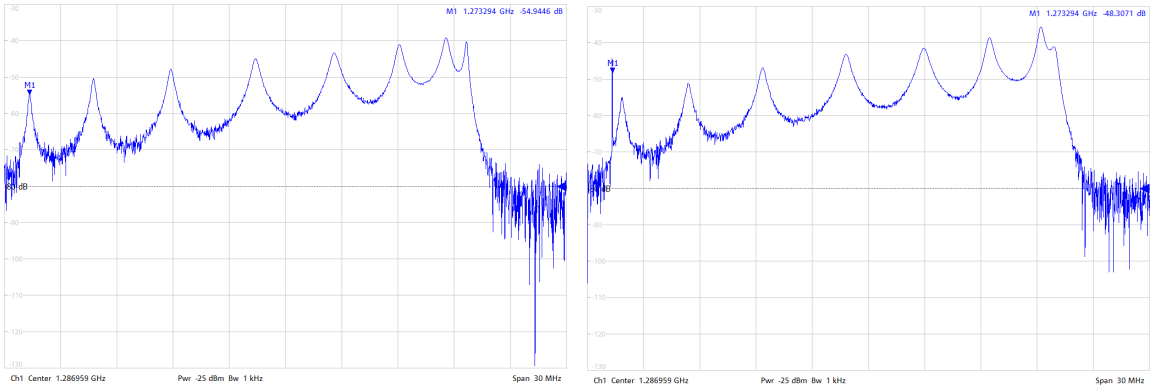

Figure 4.16: VNA S_{21} captures of the 1.3 GHz TESLA 9-cell's passband before (left) and after (right) a plasma is ignited using the $\frac{1}{9}\pi$-mode at 86 W. Here, a marker is held over the $\frac{2}{9}\pi$-mode to illustrate that a peak shift has occurred.

Table 4.3: Mode frequency shifts seen in the 1.3 GHz TESLA 9-cell when plasma is ignited using the $\frac{1}{9}\pi$-mode. Each cavity shift is in MHz.

	$\frac{1}{9}\pi$	$\frac{2}{9}\pi$	$\frac{3}{9}\pi$	$\frac{4}{9}\pi$	$\frac{5}{9}\pi$	$\frac{6}{9}\pi$	$\frac{7}{9}\pi$	$\frac{8}{9}\pi$	π
86 W	0.271	0.175	0.191	0.140	0.193	0.136	0.149	0.183	0.130
136 W	0.310	0.317	0.265	0.252	0.236	0.223	0.202	0.287	0.177

Rather than focusing on absolute magnitude of the frequency shift, this model requires that the frequency shifts are ranked based on difference. Namely, shifts with greater deviations from the initial resonant frequency would be ranked higher, with 1 being the largest shift seen for a particular plasma ignition.

A similar methodology is applied to the U_{mn} matrix, which instead ranks the magnitude of stored energy for each row. Each row assumes a specific plasma location, and provides an expected frequency ranking. Each row is compared to the experimentally determined

frequency shift data through a least-squares minimization of the form

$$\delta_m = \sqrt{\sum_m (RU_m - R_m)^2} \tag{4.1}$$

where δ_m is the least-squares minimization value, RU_m is the index of the stored energy matrix, and R_m is the equivalent index for the frequency shift data. The plasma's location is then estimated based on the minimal value produced by the least-squares analysis. One example of this procedure is shown in Appendix A, while the subsequent subsection in the Appendix summarizes the overall results of the prediction model.

Various trends were exhibited in the predicted results, making it difficult to generalize the plasma behavior. In modes like the $\frac{4}{9}\pi$-mode, the plasma is stationary regardless of the input power. Some of the results indicated that the plasma would change positions with increases to cavity power. One specific case is when the cavity is being driven by the $\frac{2}{9}\pi$-mode. Here, the plasma is seen to ignite in Cell 3 and move to Cell 7 until the 110 W mark. After this point, the plasma repositioned itself back to Cell 2, closer to the coupler. When the plasma was observed to move, there was not a clear pattern indicating favorable movements or locations. Other cases, such as the $\frac{8}{9}\pi$-mode, confined the plasma fairly locally, only repositioning from Cell 3 to Cell 5. Electric field concentrations did not appear to affect the migration of plasma to a particular cell. In fact, modes, such as the $\frac{8}{9}\pi$-mode, would transition the plasma to cells with a relatively low field concentration, comparatively. As such, it seems only the initial ignition requires a strong electric field present in the cell.

Most ignition locations were fairly consistent with the assumption that plasma would ignite at high-field cells. Any deviations from this assumption were typically seen with modes where there were several regions with comparable field magnitudes. In these cases, plasma was typically seen to choose positions closer to the coupler. Observing the results for the π-mode, neither behavior was produced. Namely, the plasma ignition was estimated to occur in a cell with a lower overall field, away from the coupler. It is not known why the model only fails in this particular mode.

At this stage, the predictive model shows some promise in its ability to estimate the plasma's physical location within the 9-cell cavity. However, the model is currently incomplete without the $\frac{1}{9}\pi$-mode data. If the impact of first mode affects the produced results even marginally, then it must not be overlooked to preserve experimental accuracy.

4.3 Cold Test

Performance changes resulting from plasma processing were measured using cold tests. A total of two tests were conducted at 4K and 2K using the 1.3 GHz single-cell SRF cavity to observe the effectiveness of plasma processing in removing hydrocarbon contaminants. The first test needed to be completed with a cavity that was considered dirty. By introducing hydrocarbon contaminants onto the cavity surface, the expected performance of the studied cavity would noticeably decrease from field emission. The second test would then act as a qualification test that focuses on removing the introduced contaminants. Ideally, the cavity performance would be recovered following plasma processing, providing us with conclusive evidence regarding the technique's effectiveness at *in-situ* cleaning.

Very careful preparations were made prior to testing to avoid the introduction of contaminants onto the inner cavity surface. Namely, the single-cell was subjected to 90 minutes of HPR and allowed to dry in a Class-10 clean room to avoid the introduction of additional particulates into the cavity environment. Following cavity assembly in a Class-10 clean room, the cavity was pumped at a rate of approximately 1 Torr/s to avoid particulate disturbances. Below 1 Torr, pumping was done with a turbo pump until Ultra-High Vacuum (UHV) conditions were reached.

To apply uniform hydrocarbon contamination within the single-cell cavity, the clean cavity was attached to a modified form of the plasma processing assembly (see Figure 4.17). Here, we attempted to control the amount of contamination placed onto the cavity surface by igniting and maintaining a 95%-5% He-CH_4 plasma. However, it was found that the variable coupler was too undercoupled to ignite a plasma capable of splitting the methane molecule into individual constituents. In fact, the RF feedthrough holding the input coupler was damaged in the process due to the lack of thermal insulation around the coupler. As such, a two-step testing approach was created. Table 4.4 summarizes the developed procedure.
In the two-step processing test, the first step was to reconfigure the plasma processing assembly back to the bench setup. This arrangement would handle the ignition and maintenance of a contamination plasma or a cleaning plasma within the cavity. Furthermore, this task would only require a swap from the variable coupler to the coupler shown in Figure 3.3. After cavity processing is completed, the cold test cavity assembly would be reinstated for the 4K and 2K testing.

Using the initial plasma processing assembly, a total of two plasmas were ignited within

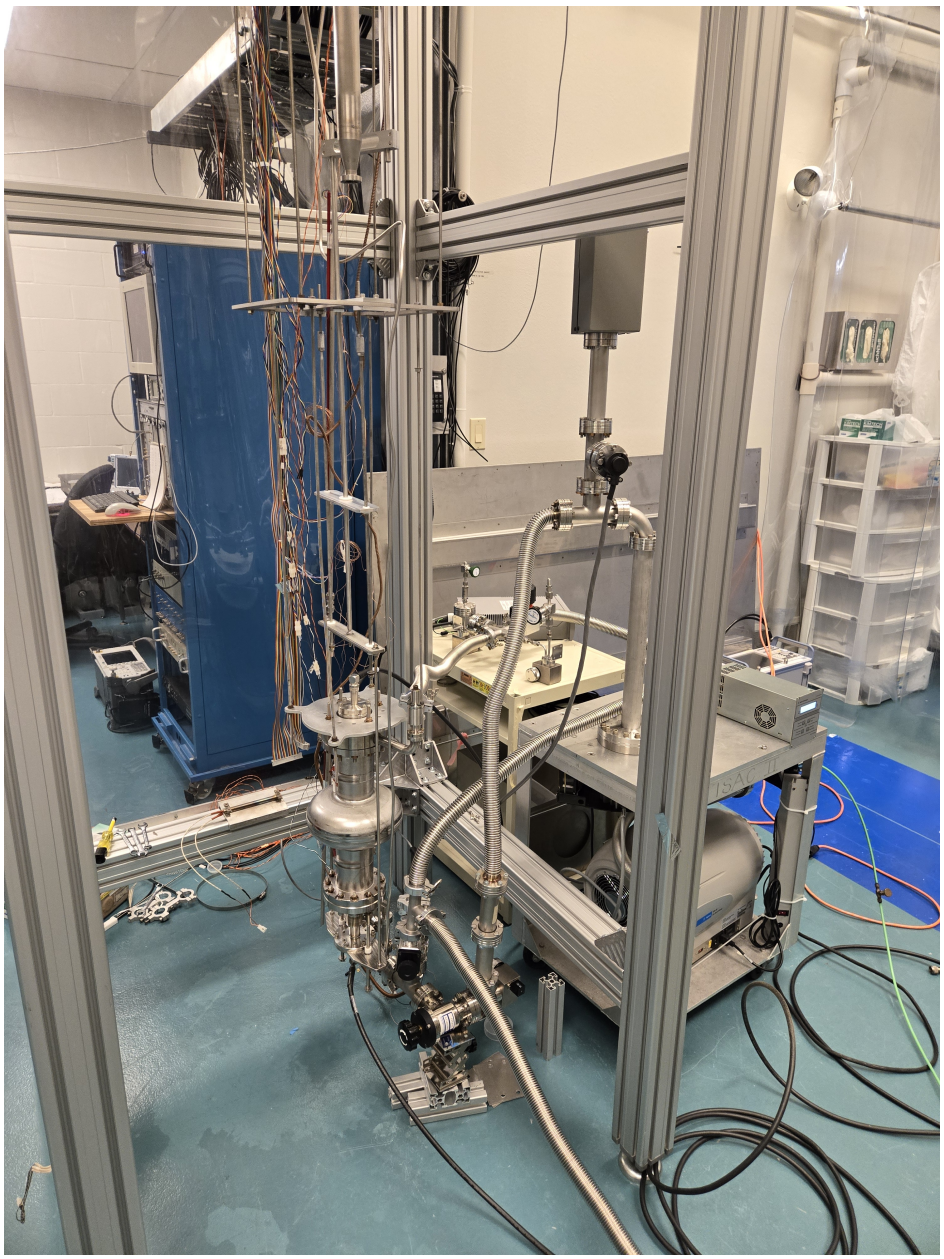

Figure 4.17: The 1.3 GHz single-cell SRF cavity suspended from the cryoinsert while attached to the modified plasma processing apparatus. Components used in the assembly, like the variable coupler or pumping cart, can be seen attached to various adapting flanges on the cavity.

Table 4.4: The generalized procedure used in the cold test experiments, detailed step by step.

Step	Details
HPR	Cavity is sprayed with deionized water to remove particulates.
Class-10 assembly	Cavity attachments are added in a controlled, clean environment.
Contamination	A He-CH_4 plasma is ignited within the cavity to contaminate it.
Slow pump and vent	Done to swap between plasma and cold test couplers.
Cold test	4K and 2K testing conducted to quantify cavity performance.
Slow pump and vent	Done to swap between plasma and cold test couplers.
Cleaning	A He-O_2 plasma is ignited within the cavity to clean it.
Slow pump and vent	Done to swap between plasma and cold test couplers.
Cold test	4K and 2K testing conducted to validate technique's capabilities.

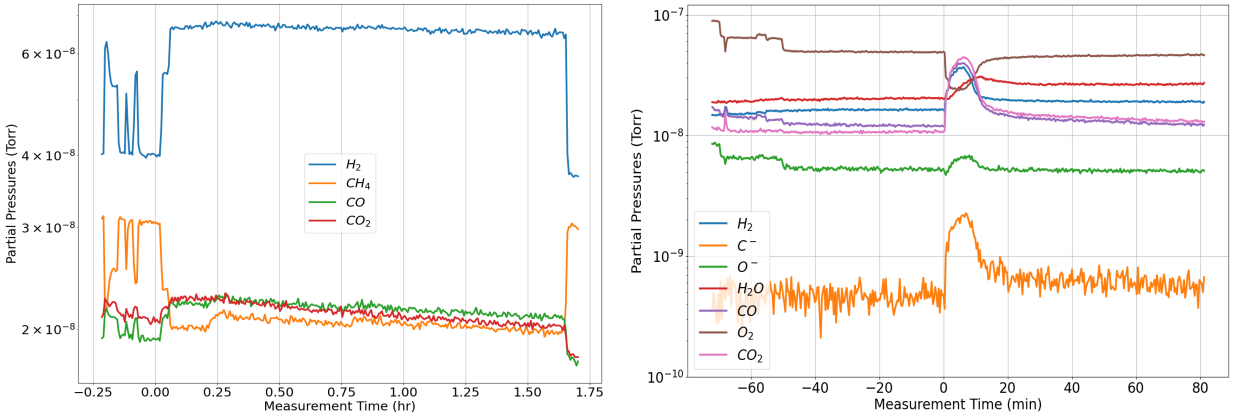

Figure 4.18: RGA PvT scans for each plasma step performed in the qualification tests. The left panel shows the byproduct responses while the He-CH_4 95%-5% 80 mTorr recipe was ignited. The right panel displays the gas compositions leaving the cavity while the He-O_2 95%-5% 80 mTorr cleaning plasma was maintained. t=0 here indicates plasma's initial ignition.

the single-cell cavity. The first was a 95%-5% He-CH_4 plasma that was used to artificially contaminate the inner surface of the single-cell cavity. The Helium-Methane plasma was maintained for a duration of 90 minutes at a cavity pressure of 80 mTorr using a forward power of 110 W. After the first round of cryogenic testing, a 95%-5% He-O_2 cleaning plasma

was maintained for 95% - 5% He-O_2 for approximately 45 minutes to remove newly introduced hydrocarbons from the interior of the single-cell cavity. RGA data was collected throughout each process. PvT plots highlighting the partial pressure versus time behavior for each processing step can be seen in Figure 4.18. The gas behavior in both cases is consistent with the trends exhibited in the bench trials. From the produced RGA data, each respective processing round seemed to have completed their respective roles adequately.

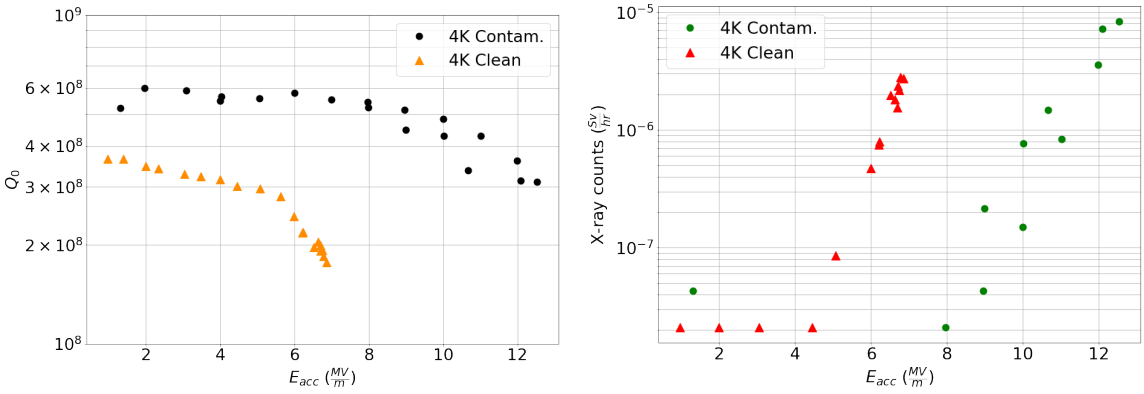

(a) 4K Q_0 vs. E_{acc}

(b) 4K X-ray counts vs. E_{acc}

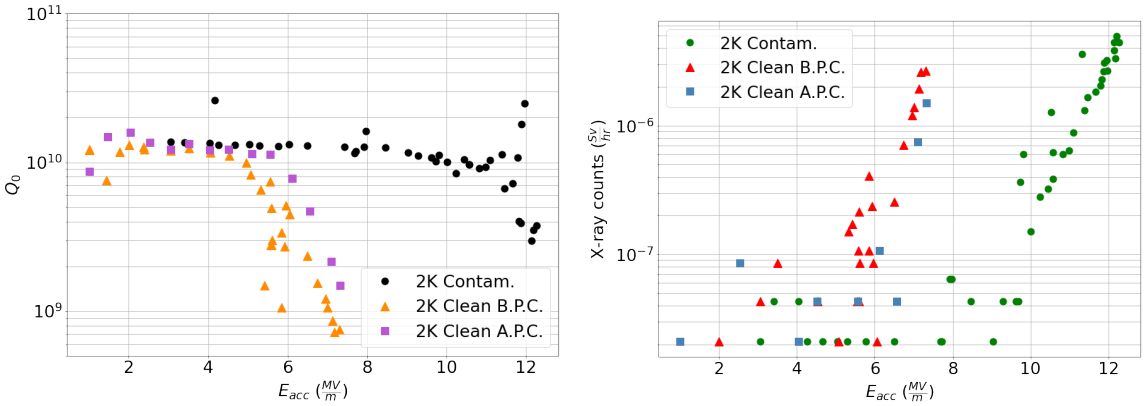

(c) 2K Q_0 vs. E_{acc}

(d) 2K X-ray counts vs. E_{acc}

Figure 4.19: Results of the cold tests conducted on the 1.3 GHz single-cell elliptical SRF cavity. Figures 4.19(a) and 4.19(c) display the Q_0 vs. E_{acc} performance of the cavity at 4K and 2K. Figures 4.19(b) and 4.19(d) plot the radiation produced from the cavity for the obtainable E_{acc} values. Note that in the 2K testing, pulse conditioning was applied in an attempt to condition the cavity. B.P.C. here corresponds to the data taken before pulse conditioning was applied, while A.P.C. refers to the data taken afterwards.

After each processing round, cryogenic tests were completed at 4K and 2K to measure the

performance changes resulting from the applied conditioning. Figure 4.19 summarizes the results from each set of tests. In the contamination test, quality factor degradation was first noted around 4 MV/m. At the time, this was believed to be due to multipacting. As such, a brief round of RF conditioning was applied, and the quality factor was recovered thereafter. The quality factor was again seen to degrade around 8 MV/m. The decrease seen was very gradual and indicative of field emission onset as X-ray counts increased corresponding to quality factor decreases. Ultimately, both the 4K and 2K tests reached a gradient around 12.5 MV/m before the X-ray radiation levels reached administrative limits. In the processed cavity, the quality factor was seen to drop significantly around 5.7 MV/m and 5.2 MV/m in the 4K and 2K tests, respectively. X-rays were also seen to spike at these gradients, quickly emulating the radiation levels seen around 12.5 MV/m in the contaminated test. The sharp downward trend suggests a strong presence of field emitters within the cavity at the time of measurement. Pulse conditioning was applied at 5.5 MV/m for 45 minutes to improve cavity performance. The curve corresponding to post-pulse conditioning performance is purple in 4.19(c). Immediately, it is seen that there were minimal improvements in the gradient, with quality factor degradation now occurring at 6 MV/m. The cavity performance observed in the contaminated cavity surpassed the processed cavity. Therefore, no conclusive evidence was produced that would indicate the effectiveness of plasma processing in promoting cavity performance.

The second cold test exhibited cavity performance significantly poorer than that found in the first cold test. It is evident that the performance degradation was due to a heightened abundance of field emitters that were present in the cavity's RF environment. Although the source is not exactly known, we speculate that there were several procedural choices that could have introduced new contaminates into the cavity, moved existing contaminants into higher RF regions within the cavity, or both. One such example is that if the gas flow rate was set too high, the injected gases would disrupt the settled particulates. Among the several reasons, the transfer of couplers was likely the main reason for the performance degradation. Specifically, our remedy for the inability of the variable coupler to ignite plasma was to change the coupler during processing intervals. In each coupler swap, the cavity needed to be vented, exposing the cavity to the gas present in our slowing pumping/venting system. The cleanliness of our slow pumping and venting system was tested in a separate series of cold tests. Q_0 versus E_{acc} plots at 4K and 2K (see Figures 4.20(a) and 4.20(b)) show that the cavities vented by this system experienced contamination around the same point at which the plasma processing qualification tests first saw performance degradation, 10 MV/m. In

short, the slow venting and pumping system was compromised with contaminates. A total of four cavity vents were completed, creating four instances where new contaminants could have been introduced into the cavity. Of the four cavity vents, the final iteration was likely the primary candidate for the performance degradation seen in the second cold test, as it is the only step that displayed results that deviated from expectation. No changes were made to the venting procedure in this last step, so it is hard to say if the degradation was purely the effect of an influx of new contaminants within the cavity.

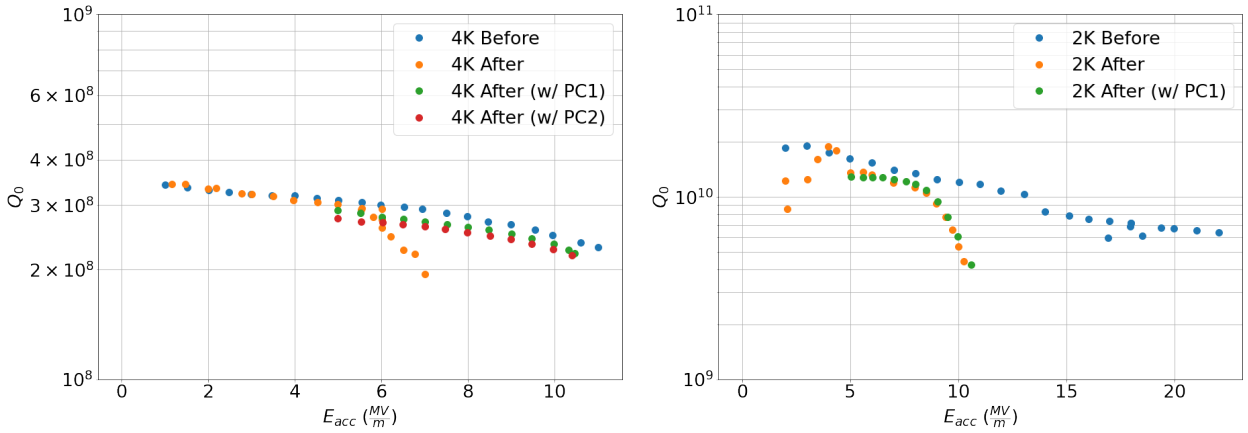

(a) 4K Q_0 vs. E_{acc}

(b) 2K Q_0 vs. E_{acc}

Figure 4.20: Results of the cold tests conducted on the 1.3 GHz single-cell elliptical SRF cavity to qualify our slow vent/pump system. Figures 4.20(a) and 4.20(b) display the Q_0 vs. E_{acc} performance of the cavity at 4K and 2K, respectively. In the 2K testing, pulse conditioning was applied in several iterations to condition the cavity. B.P.C. PC1 refers to the first round of pulse conditioning, while PC2 refers to the second.

Before further plasma processing cryogenic testing is attempted, a modified variable coupler should be developed that allows for further penetration into the cavity. When within the cryostat, the coupler should function exactly as the current variable coupler. The primary differences would be for room temperature conditioning. Specifically, a system near critical coupled is needed to efficiently ignite the plasma. By extending the coupler length, there would be more flexibility in creating the ideal coupling conditions. Furthermore, not having to alternate between couplers removes the necessity for several cavity vents, reducing the potential contamination risk.

Chapter 5

Conclusions and Future Work

Conclusions

Plasma processing is an *in-situ* cleaning technique that has found success in restoring the on-line performance of SRF cavities at several linac facilities. In this technique, a plasma is ignited within the cavity to chemically remove hydrocarbon field emitters on the inner cavity surface. The focus of this thesis was to better understand the plasma ignition mechanisms within 1.3 GHz SRF cavities in preparation of an eventual roll-out onto TRIUMF's ARIEL eLINAC.

In Section 4.2.1., plasma's effectiveness at removing hydrocarbons was demonstrated within a 1.3 GHz single-cell cavity. Plasma testing at this stage attempted to optimize plasma cleaning by exploring processing parameters. Initially, several inert gases were used to process the single-cell cavity. He-O_2 plasmas were found to produce RGA byproduct curves most consistent with literature. Further refinement of the gas recipe warranted the need for artificial pollution using a He-CH_4 plasma. By alternating between a contamination plasma and a cleaning plasma, hydrocarbon removal between gas recipes was tested. Ultimately, it was found that the combination of a lower Oxygen gas ratio and lower cavity pressure was the most effective in removing byproducts. Due to equipment limitations, 5% O_2 and 80 mTorr was the lowest achievable threshold for either parameter. Further parameter exploration is intended before it can be concluded that the presented recipe is the optimized cleaning procedure.

The beadpull measurements shown in Section 4.1. provided information into how plasma traverses through the multi-cell cavities for each driving mode. Through these plots, it was

discovered that one of the multi-cell cavities, the 1.3 GHz 5-cell ARIEL RF cavity, did not exhibit coherent π-mode behavior. By simulating the cavity in Poisson SUPERFISH, it was determined that the cavity was fundamentally flawed, presently making representative modal studies in ARIEL multi-cell cavities impossible.

Plasma movement in both multi-cell cavities was confirmed using S_{21} responses from the VNA. In the case of the 5-cell, plasma locations were verified using an on-axis optical window. Surprisingly, the plasma location exactly followed the points with the highest electric field magnitude for each driving mode. As such, a model was proposed in Section 4.2.3. which utilized the beadpull distributions to estimate the ignition location of plasma for the various driving modes. The model produced fairly consistent results. However, it is currently incomplete as the stored energy data for the $\frac{1}{9}\pi$-mode was not collected due to transmission issues on the beadpull bench. Plans are in place to acquire this data and complete the model.

Finally, shown in Section 4.3., a series of 4K and 2K cold tests were conducted to qualify plasma processing. The cavity, when polluted, was able to reach 11 MV/m before we recorded field emission onset. After subjecting the cavity to a round of plasma processing, the performance decreased to only 6 MV/m. We believe that the degradation in cavity performance was due to procedural choices. Currently, we cannot make a conclusive statement regarding the effectiveness of plasma processing without repeating the 4K and 2K testing.

Future Work

At this stage of development, plasma processing cannot be applied on-line. There are several milestones that still need to be achieved experimentally. The results presented in this dissertation have provided valuable insight into discerning how to achieve these goals going forward and how to improve our existing apparatus and procedure.

In Section 4.2.1., it was shown that the contamination levels across each of the processing tests were unequal, suggesting the implementation of mass flow controllers to regulate flow and reduce the risk of particulate displacement. Coupler ignition was seen to limit the achievable plasma density in Section 4.2.2. To mitigate this, rather than using power changes, the driving frequency will follow the resonance, maintaining the coupling to the plasma.

Improvements to the existing procedure cannot account for the differences between the bench and cryomodule assemblies. As such, future plasma studies aim to bridge this gap by recreating the cryomodule environment off-line. A flattened 1.3 GHz ARIEL 9-cell SRF cavity must be tested with the 50 kW FPCs used within the cryomodules to understand how substantially undercoupled systems ignite plasma in these particular cavities.

Eventually, the plasma processing assembly must be transitioned from a fixed apparatus to a mobile cart. Plans are in place to install a second accelerating cryomodule to ARIEL's beamline, pushing the final energy to 50 MeV [51]. Making the plasma processing assembly mobile improves its accessibility, enabling the possibility of repeated processing for each cryomodule, without significant changes to their configuration. Only simple vacuum connections will be needed to prepare a cryomodule for the plasma processing cart.

Appendix A

Appendix

Mode Shift Data

Resonant modes in the fundamental passband shift as a consequence of plasma ignition. This subsection summarizes the frequency shifts seen in the nine modes when driving the cavity fields with each of the different modes. Tables are organized so that each column corresponds to a particular resonant peak's shift following plasma ignition. Rows here describe the plasma power at the time of measurement.

Table A.1: Mode frequency shifts measured for several powers when a plasma is ignited using the $\frac{1}{9}\pi$-mode. Each cavity shift is in MHz.

	$\frac{1}{9}\pi$	$\frac{2}{9}\pi$	$\frac{3}{9}\pi$	$\frac{4}{9}\pi$	$\frac{5}{9}\pi$	$\frac{6}{9}\pi$	$\frac{7}{9}\pi$	$\frac{8}{9}\pi$	π
86 W	0.271	0.175	0.191	0.140	0.193	0.136	0.149	0.183	0.130
136 W	0.310	0.317	0.265	0.252	0.236	0.223	0.202	0.287	0.177

Table A.2: Mode frequency shifts measured for several powers when a plasma is ignited using the $\frac{2}{9}\pi$-mode. Each cavity shift is in MHz.

	$\frac{1}{9}\pi$	$\frac{2}{9}\pi$	$\frac{3}{9}\pi$	$\frac{4}{9}\pi$	$\frac{5}{9}\pi$	$\frac{6}{9}\pi$	$\frac{7}{9}\pi$	$\frac{8}{9}\pi$	π
25 W	0.192	0.371	0.115	0.099	0.237	0.271	0.023	0.067	0.079
45 W	0.308	0.505	0.160	0.280	0.266	0.342	0.150	0.123	0.533
75 W	0.428	0.513	0.210	0.447	0.367	0.457	0.304	0.123	0.727
110 W	0.193	0.566	0.840	0.773	0.663	0.661	0.607	0.894	0.778

Table A.3: Mode frequency shifts measured for several powers when a plasma is ignited using the $\frac{3}{9}\pi$-mode. Each cavity shift is in MHz. Here, N/M means that the the resonant peak could not be measured once plasma was ignited.

	$\frac{1}{9}\pi$	$\frac{2}{9}\pi$	$\frac{3}{9}\pi$	$\frac{4}{9}\pi$	$\frac{5}{9}\pi$	$\frac{6}{9}\pi$	$\frac{7}{9}\pi$	$\frac{8}{9}\pi$	π
37 W	0.075	0.306	0.546	0.475	0.338	0.272	0.415	0.621	0.170
61 W	0.075	0.373	0.701	0.704	0.530	0.460	0.581	0.756	0.371
97 W	0.075	0.428	0.837	0.938	0.810	0.741	0.816	0.872	N/M

Table A.4: Mode frequency shifts measured for several powers when a plasma is ignited using the $\frac{4}{9}\pi$-mode. Each cavity shift is in MHz. Here, N/M means that the the resonant peak could not be measured once plasma was ignited.

	$\frac{1}{9}\pi$	$\frac{2}{9}\pi$	$\frac{3}{9}\pi$	$\frac{4}{9}\pi$	$\frac{5}{9}\pi$	$\frac{6}{9}\pi$	$\frac{7}{9}\pi$	$\frac{8}{9}\pi$	π
45 W	0.601	0.441	0.167	0.866	0.126	0.434	0.752	-0.019	0.826
61 W	0.695	0.516	0.355	0.994	0.215	0.510	0.884	0	1.032
79 W	0.964	0.595	0.664	1.168	0.471	0.650	1.059	0.049	1.387

Table A.5: Mode frequency shifts measured for several powers when a plasma is ignited using the $\frac{5}{9}\pi$-mode. Each cavity shift is in MHz. Here, N/M means that the the resonant peak could not be measured once plasma was ignited.

	$\frac{1}{9}\pi$	$\frac{2}{9}\pi$	$\frac{3}{9}\pi$	$\frac{4}{9}\pi$	$\frac{5}{9}\pi$	$\frac{6}{9}\pi$	$\frac{7}{9}\pi$	$\frac{8}{9}\pi$	π
39 W	0.021	0.167	0.402	0.581	0.744	0.934	1.016	N/M	1.324
51 W	0.036	0.182	0.951	0.655	0.824	1.013	1.090	0.778	N/M
65 W	0.505	1.571	0.456	0.440	1.330	1.084	0.179	0.930	N/M

Table A.6: Mode frequency shifts measured for several powers when a plasma is ignited using the $\frac{6}{9}\pi$-mode. Each cavity shift is in MHz. Here, N/M means that the the resonant peak could not be measured once plasma was ignited.

	$\frac{1}{9}\pi$	$\frac{2}{9}\pi$	$\frac{3}{9}\pi$	$\frac{4}{9}\pi$	$\frac{5}{9}\pi$	$\frac{6}{9}\pi$	$\frac{7}{9}\pi$	$\frac{8}{9}\pi$	π
73 W	0.072	0.241	0.554	0.791	0.983	1.189	1.250	0.982	N/M
110 W	0.072	0.290	0.644	0.916	1.133	1.339	1.356	0.976	N/M
132 W	0.089	0.306	0.683	0.977	1.207	1.401	1.400	1.009	N/M
157 W	0.091	0.323	0.727	1.042	1.265	1.456	1.428	1.008	N/M

Table A.7: Mode frequency shifts measured for several powers when a plasma is ignited using the $\frac{7}{9}\pi$-mode. Each cavity shift is in MHz. Here, N/M means that the the resonant peak could not be measured once plasma was ignited.

	$\frac{1}{9}\pi$	$\frac{2}{9}\pi$	$\frac{3}{9}\pi$	$\frac{4}{9}\pi$	$\frac{5}{9}\pi$	$\frac{6}{9}\pi$	$\frac{7}{9}\pi$	$\frac{8}{9}\pi$	π
113 W	N/M	1.054	2.269	3.303	3.846	3.879	3.311	N/M	1.458
137 W	N/M	1.084	2.269	3.303	3.856	3.896	3.311	N/M	1.729
167 W	N/M	1.084	2.269	3.327	3.866	3.896	3.311	N/M	1.952

Table A.8: Mode frequency shifts measured for several powers when a plasma is ignited using the $\frac{8}{9}\pi$-mode. Each cavity shift is in MHz. Here, N/M means that the the resonant peak could not be measured once plasma was ignited.

	$\frac{1}{9}\pi$	$\frac{2}{9}\pi$	$\frac{3}{9}\pi$	$\frac{4}{9}\pi$	$\frac{5}{9}\pi$	$\frac{6}{9}\pi$	$\frac{7}{9}\pi$	$\frac{8}{9}\pi$	π
75 W	N/M	1.604	N/M	0.162	1.603	2.668	N/M	N/M	0.309
109 W	N/M	1.608	2.222	1.556	2.001	2.786	N/M	1.080	0.748
157 W	N/M	1.621	2.285	1.658	2.044	2.808	N/M	1.080	0.808

Table A.9: Mode frequency shifts measured for several powers when a plasma is ignited using the π-mode. Each cavity shift is in MHz. Here, N/M means that the the resonant peak could not be measured once plasma was ignited.

	$\frac{1}{9}\pi$	$\frac{2}{9}\pi$	$\frac{3}{9}\pi$	$\frac{4}{9}\pi$	$\frac{5}{9}\pi$	$\frac{6}{9}\pi$	$\frac{7}{9}\pi$	$\frac{8}{9}\pi$	π
98 W	N/M	1.177	2.076	3.068	3.409	3.278	N/M	0.152	0.567
121 W	N/M	1.177	2.083	3.068	3.439	3.301	N/M	0.156	0.645
144 W	N/M	1.187	2.083	3.092	3.439	3.323	N/M	0.160	0.955

Model Example

Shown here is an example of how the model presented in Section 4.2.3. can be used to determine the location of the plasma within the 9-cell cavity. In this example, the $\frac{4}{9}\pi$-mode is applied to the estimation model to showcase the calculation procedure.

First, the data presented in Tables 4.2 and A.4 must be converted to ranked form so that a least squares minimization can be applied. Here, the frequency data is ranked according to the difference between the resonant frequencies before and after plasma ignition. Furthermore, the stored energy matrix, U_{mn}, is ranked based on the magnitude of the column value. In either case, the largest value is given a rank of "1", with increasingly smaller values labeled in ascending order. The two ranked matrices correspond to Tables A.10 and A.11.

Table A.10: The ranked stored energy matrix for the 1.3 GHz TESLA 9-cell SRF cavity. Ranks of 1 correspond to the cells with the largest stored energy, while a rank of 9 is the lowest, comparatively.

	$\frac{2}{9}\pi$	$\frac{3}{9}\pi$	$\frac{4}{9}\pi$	$\frac{5}{9}\pi$	$\frac{6}{9}\pi$	$\frac{7}{9}\pi$	$\frac{8}{9}\pi$	π
Cell 1	7	8	6	3	4	2	1	5
Cell 2	4	1	3	8	5	7	2	6
Cell 3	2	6	7	1	4	8	3	5
Cell 4	3	7	1	8	4	2	6	5
Cell 5	6	1	8	2	4	3	7	5
Cell 6	3	6	1	8	4	2	7	5
Cell 7	2	7	6	1	4	8	5	3
Cell 8	3	1	2	7	6	8	4	5
Cell 9	7	8	5	4	6	2	1	3

Now that both matrices are in a ranked format, each row in the frequency shift matrix will be iteratively tested against each row of the stored energy matrix through a least-squares minimization. In other words, each unique power row in Table A.11 will be applied to Equation 4.1 against the nine stored energy rows in Table A.10 to produce nine minimization values. The likely position of plasma is then determined by the smallest minimization value. Analytically, this calculation is shown below for the 45 W row of frequency shift data and

Table A.11: The ranked frequency shift matrix produced from plasma ignition using the $\frac{4}{9}\pi$-mode. Columns specify which resonant mode the shift refers to, while the rows denote the cavity power for each ignited plasma.

	$\frac{1}{9}\pi$	$\frac{2}{9}\pi$	$\frac{3}{9}\pi$	$\frac{4}{9}\pi$	$\frac{5}{9}\pi$	$\frac{6}{9}\pi$	$\frac{7}{9}\pi$	$\frac{8}{9}\pi$	π
45 W	4	5	7	1	8	6	3	9	2
61 W	4	5	7	1	8	6	3	9	1
79 W	4	7	5	2	8	6	3	9	1

for the Cell 1 row in the stored energy matrix:

$$\begin{aligned} & \delta_m^2 = \sum_m (RU_m - R_m)^2 \\ & \delta_m^2 = (7-5)^2 + (8-7)^2 + ... + (1-9)^2 + (5-2)^2 \\ & \delta_m^2 = 133 \\ \rightarrow \quad & \delta_m = 11.532 \approx 12 \end{aligned}$$

The results of applying the least squares minimization to Table A.11 is summarized in Table A.12. Note that the values presented refer to δ_m^2, rather than δ_m for additional clarity.

Examining each column, the model appears to predict that the plasma is located in Cell 7 in all three cases. Each column produces minimization values that are marginally lower than those seen with the next closest prediction, Cell 4. This suggests that, at the time of testing, the plasma was located in either Cell 4 or 7, with a slight preference for the latter. Recalling the $\frac{4}{9}\pi$-mode's beadpull plot, Cells 4 and 7 hold the highest field amplitude, so the result produced is consistent with initial expectation.

Table A.12: The square of the least-squares minimization values, δ_m^2, for the three experimentally acquired frequency shift data sets. Values highlighted in blue represent the most likely estimation of the plasma's location during testing.

	45 W	61 W	79 W
Cell 1	133	140	135
Cell 2	123	132	117
Cell 3	169	176	181
Cell 4	27	34	51
Cell 5	139	146	113
Cell 6	54	67	64
Cell 7	23	30	43
Cell 8	101	108	99
Cell 9	103	106	103

Plasma Location Matrices

Each of the frequency shift data sets presented above were input into the frequency prediction model. The following Section summarizes the findings of this model in a manner similar to Table A.12, sequentially.

Table A.13: δ_m^2 values for the $\frac{2}{9}\pi$ driving mode. Presented are the plasma location predictions for four power levels.

	25 W	45 W	75 W	110 W
Cell 1	132	157	144	75
Cell 2	108	123	136	48
Cell 3	46	77	92	123
Cell 4	100	79	66	73
Cell 5	76	125	134	49
Cell 6	95	104	101	59
Cell 7	94	75	64	67
Cell 8	94	93	106	57
Cell 9	162	151	132	63

Table A.14: δ_m^2 values for the $\frac{3}{9}\pi$ driving mode. Presented are the plasma location predictions for three power levels.

	35 W	62 W	97 W
Cell 1	72	69	67
Cell 2	32	42	43
Cell 3	102	107	89
Cell 4	94	56	64
Cell 5	90	59	53
Cell 6	75	40	47
Cell 7	96	47	55
Cell 8	50	50	44
Cell 9	72	71	59

Table A.15: δ_m^2 values for the $\frac{5}{9}\pi$ driving mode. Presented are the plasma location predictions for three power levels.

	45 W	62 W	79 W
Cell 1	23	15	107
Cell 2	108	100	84
Cell 3	91	91	11
Cell 4	66	63	123
Cell 5	57	63	65
Cell 6	102	79	125
Cell 7	65	69	121
Cell 8	120	125	73
Cell 9	17	25	121

Table A.16: δ_m^2 values for the $\frac{6}{9}\pi$ driving mode. Presented are the plasma location predictions for four power levels.

	75 W	110 W	132 W	157 W
Cell 1	19	19	19	33
Cell 2	91	112	112	110
Cell 3	83	87	87	87
Cell 4	52	67	67	61
Cell 5	41	53	53	57
Cell 6	65	83	83	69
Cell 7	49	71	71	63
Cell 8	110	131	131	123
Cell 9	29	31	31	47

Table A.17: δ_m^2 values for the $\frac{7}{9}\pi$ driving mode. Presented are the plasma location predictions for three power levels.

	110 W	137 W	167 W
Cell 1	72	72	72
Cell 2	91	91	91
Cell 3	62	62	62
Cell 4	68	68	68
Cell 5	43	43	43
Cell 6	72	72	72
Cell 7	62	62	62
Cell 8	78	78	78
Cell 9	90	90	90

Table A.18: δ_m^2 values for the $\frac{8}{9}\pi$ driving mode. Presented are the plasma location predictions for three power levels.

	110 W	137 W	167 W
Cell 1	36	84	90
Cell 2	53	63	69
Cell 3	18	50	64
Cell 4	52	80	74
Cell 5	36	29	29
Cell 6	93	76	68
Cell 7	52	72	64
Cell 8	52	60	60
Cell 9	52	112	112

Table A.19: δ_m^2 values for the π driving mode. Presented are the plasma location predictions for three power levels.

	110 W	137 W	167 W
Cell 1	74	74	74
Cell 2	93	93	93
Cell 3	50	50	50
Cell 4	72	72	72
Cell 5	41	41	41
Cell 6	78	78	78
Cell 7	66	66	66
Cell 8	76	76	76
Cell 9	94	94	94

Bibliography

[1] J. Dilling, R. Krücken, and G. Ball, *ISAC overview*, pp. 1–8. Dordrecht: Springer Netherlands, 2014.

[2] S. R. Koscielniak *et al.*, "Electron Linac Photo-fission Driver for the Rare Isotope Program at TRIUMF," in *Proc. IPAC'10*, no. 1 in International Particle Accelerator Conference, pp. 4275–4277, JACoW Publishing, Geneva, Switzerland, 2010.

[3] W. T. Diamond, "A radioactive ion beam facility using photofission," *Nuclear Instruments and Methods in Physics Research Section A: Accelerators, Spectrometers, Detectors and Associated Equipment*, vol. 432, no. 2, pp. 471–482, 1999.

[4] R. E. Laxdal *et al.*, "The 30MeV Stage of the ARIEL e-linac," in *Proc. SRF'17*, no. 18 in International Conference on RF Superconductivity, pp. 6–12, JACoW Publishing, Geneva, Switzerland, 2017.

[5] P. G. Bricault, F. Ames, M. Dombsky, V. Hanemaayer, P. Kunz, and J. Lassen, "Progress towards New RI and Higher RIB Intensities at TRIUMF," in *Proc. Cyclotrons'10*, no. 19 in International Conference on Cyclotrons and their Applications, pp. 365–370, JACoW Publishing, Geneva, Switzerland.

[6] P. Kneisel, B. Lewis, and L. Turlington, "Experience with High Pressure Ultrapure Water Rinsing of Niobium Cavities," in *Proc. SRF'93*, no. 6 in Workshop on RF Superconductivity, JACoW Publishing, Geneva, Switzerland.

[7] H. Padamsee, "50 years of success for srf accelerators – a review," *Superconductor Science and Technology*, vol. 30, 2017.

[8] B. Bonin, "Field emission in RF cavities," in *ICTP School on Nonaccelerator Particle Astrophysics*, pp. 221–230, 1995.

[9] M. Doleans *et al.*, "Plasma Processing R&D for the SNS Superconducting Linac RF Cavities," in *Proc. SRF'13*, no. 16 in International Conference on RF Superconductivity, pp. 551–557, JACoW Publishing, Geneva, Switzerland.

[10] M. Doleans, P. Tyagi, R. Afanador, C. McMahan, J. Ball, D. Barnhart, W. Blokland, M. Crofford, B. Degraff, S. Gold, B. Hannah, M. Howell, S.-H. Kim, S.-W. Lee, J. Mammosser, T. Neustadt, J. Saunders, S. Stewart, W. Strong, D. Vandygriff, and D. Vandygriff, "In-situ plasma processing to increase the accelerating gradients of superconducting radio-frequency cavities," *Nuclear Instruments and Methods in Physics Research Section A: Accelerators, Spectrometers, Detectors and Associated Equipment*, vol. 812, pp. 50–59, 2016.

[11] M. Doleans, "Ignition and monitoring technique for plasma processing of multicell superconducting radio-frequency cavities," *Journal of Applied Physics*, vol. 120, p. 243301, 12 2016.

[12] P. Berrutti *et al.*, "Update on Plasma Processing RD for LCLS-II," in *Proc. IPAC'18*, no. 9 in International Particle Accelerator Conference, pp. 2656–2658, JACoW Publishing, Geneva, Switzerland, 2018.

[13] B. Giaccone *et al.*, "Plasma Processing to Reduce Field Emission in LCLS-II 1.3 GHz SRF Cavities," in *Proc. SRF'19*, no. 19 in International Conference on RF Superconductivity, pp. 1231–1238, JACoW Publishing, Geneva, Switzerland.

[14] B. Aune, R. Bandelmann, D. Bloess, B. Bonin, A. Bosotti, M. Champion, C. Crawford, G. Deppe, B. Dwersteg, D. A. Edwards, H. T. Edwards, M. Ferrario, M. Fouaidy, P.-D. Gall, A. Gamp, A. Gössel, J. Graber, D. Hubert, M. Hüning, M. Juillard, T. Junquera, H. Kaiser, G. Kreps, M. Kuchnir, R. Lange, M. Leenen, M. Liepe, L. Lilje, A. Matheisen, W.-D. Möller, A. Mosnier, H. Padamsee, C. Pagani, M. Pekeler, H.-B. Peters, O. Peters, D. Proch, K. Rehlich, D. Reschke, H. Safa, T. Schilcher, P. Schmüser, J. Sekutowicz, S. Simrock, W. Singer, M. Tigner, D. Trines, K. Twarowski, G. Weichert, J. Weisend, J. Wojtkiewicz, S. Wolff, and K. Zapfe, "Superconducting tesla cavities," *Phys. Rev. ST Accel. Beams*, vol. 3, p. 092001, Sep 2000.

[15] P. U. Kolb, *The TRIUMF nine-cell SRF cavity for ARIEL.* PhD thesis, University of British Columbia, 2016.

[16] D. J. Griffiths, *Introduction to Electrodynamics - 4th Edition.* Pearson Education, 2017.

[17] R. Bailey, "Cas - cern accelerator school: Course on superconductivity for accelerators," 2014.

[18] H. Padamsee, J. Knobloch, and T. Hays, *RF Superconductivity for Accelerators*. Wiley, 1998.

[19] J. S. McCarthy and R. R. Whitney, eds., *Proceedings, Conference on Future Possibilities for Electron Accelerators, Charlottesville, USA, 8 - 10 Jan 1979*, Virginia U., 1979.

[20] C. Pagani, D. Barni, A. Bosotti, P. Pierini, and G. Ciovati, "Design criteria for elliptical cavities," in *Proceedings of the 10th Workshop on RF Superconductivity*, 2001.

[21] J. K. Sekutowicz, "Superconducting elliptical cavities," in *CERN Accelerator School: Course on RF for Accelerators*, 1 2012.

[22] N. R. A. Valles and M. Liepe, "The Superheating Field of Niobium: Theory and Experiment," in *Proc. SRF'11*, no. 15 in International Conference on RF Superconductivity, pp. 293–301, JACoW Publishing, Geneva, Switzerland.

[23] S. Belomestnykh and V. Shemelin, "High-β Cavity Design - A Tutorial," in *Proc. SRF'05*, no. 12 in International Workshop on RF Superconductivity, pp. 2–19, JACoW Publishing, Geneva, Switzerland.

[24] O. H. K., "The superconductivity of mercury," *Comm. Phys. Lab. Univ. Leiden*, vol. 122, p. 124, 1911.

[25] A. M. Forrest, "Meissner and ochsenfeld revisited," *European Journal of Physics*, vol. 4, p. 117, apr 1983.

[26] J. Bardeen, L. N. Cooper, and J. R. Schrieffer, "Theory of superconductivity," *Phys. Rev.*, vol. 108, pp. 1175–1204, Dec 1957.

[27] P. Cayado, "Preparation of gdba2cu3o7 superconducting films by chemical solution deposition," Master's thesis, Universitat Autònoma de Barcelona, 2012.

[28] R. Parodi, "Multipacting," *CAS 2010 - CERN Accelerator School: RF for Accelerators, Proceedings*, 12 2011.

[29] R. H. Fowler and L. W. Nordheim, "Electron emission in intense electric fields," *Proceedings of The Royal Society A: Mathematical, Physical and Engineering Sciences*, vol. 119, pp. 173–181, 1928.

[30] D. S. Joag1, M. A. More1, and F. J. Sheini, "Field emission from nanowires," in *Nanowires* (A. Hashim, ed.), ch. 24, Rijeka: IntechOpen, 2011.

[31] J. D. Getty and D. Chir, "Plasma process considerations in emerging semiconductor packaging technologies," in *2010 34th IEEE/CPMT International Electronic Manufacturing Technology Symposium (IEMT)*, pp. 1–4, 2010.

[32] J. Sun, Y. Yu, J. Tang, Y. Zeng, and J. Chen, "Plasma cleaning technology: Mechanisms, influencing factors, and applications," *IEEE Access*, vol. PP, pp. 1–1, 01 2025.

[33] P. V. Tyagi, M. Doleans, S.-H. Kim, R. Afanador, and C. J. McMahan, "Plasma Processing of Nb Surfaces for SRF Cavities," in *Proc. LINAC'14*, no. 27 in Linear Accelerator Conference, pp. 323–325, JACoW Publishing, Geneva, Switzerland, 12 2014.

[34] T. Powers, N. Brock, and T. Ganey, "In Situ Plasma Processing of Superconducting Cavities at JLab," in *Proc. NAPAC'22*, no. 5 in International Particle Accelerator Conference, pp. 22–25, JACoW Publishing, Geneva, Switzerland, 10 2022.

[35] A. D. Wu *et al.*, "Vertical Test Results of Plasma In-situ Cleaning on Low Beta HWR Cavity," in *Proc. LINAC'18*, no. 29 in Linear Accelerator Conference, pp. 408–411, JACoW Publishing, Geneva, Switzerland, 1 2019.

[36] F. Chen, *Introduction to Plasma Physics and Controlled Fusion: Volume 1: Plasma Physics*. Springer US, 2013.

[37] K. G. Xu, "Plasma sheath behavior and ionic wind effect in electric field modified flames," *Combustion and Flame*, vol. 161, no. 6, pp. 1678–1686, 2014.

[38] T. Powers, N. Brock, and T. Ganey, "Plasma processing of srf cavities at jefferson lab," Thomas Jefferson National Accelerator Facility (TJNAF), Newport News, VA (United States), 08 2022.

[39] K. Jousten, "Iso standards for vacuum metrology," in *Proc. IMEKO TC16*, no. 7 in International Conference on Pressure and Vacuum Metrology, IMEKO TC16, 5 2023.

[40] P. Kolb, B. Amini, R. E. Laxdal, Y. Ma, Z. Y. Yao, and V. Zvyagintsev, "Measuring the Higher Order Mode Spectrum of the TRIUMF 9-cell Cavity," in *Proc. SRF'13*, no. 17 in International Conference of RF Superconductivity, pp. 936–938, JACoW Publishing, Geneva, Switzerland.

[41] F. Furuta and K. Saito, "Field Flatness Degradation Problems and Cure," in *Proc. SRF'09*, no. 14 in International Conference of RF Superconductivity, pp. 818–820, JACoW Publishing, Geneva, Switzerland.

[42] A. Koveshnikov, R. Laxdal, I. Sekachev, and D. Yosifov, "Vertical test cryostat for scrf cavities testing below 2.17 k with closed loop helium circulation," in *ICEC 23*, no. 23 in International Cryogenic Engineering Conference, 06 2010.

[43] K. Fong, M. Laverty, and S. Fang, "RF Control System for ISAC II Superconducting Cavity Test Stand," in *Proc. LINAC'02*, no. 21 in Linear Accelerator Conference, pp. 701–703, JACoW Publishing, Geneva, Switzerland.

[44] "Comsol multiphysics® v. 6.3.," 2024.

[45] M. T. Menzel and H. K. Stokes, "User's guide for the poisson/superfish group of codes," 1 1987.

[46] P. Kolb, R. E. Laxdal, Y. Ma, Z. Y. Yao, and V. Zvyagintsev, "HOM Measurements on the ARIEL eLINAC Cryomodules," in *Proc. SRF'15*, no. 17 in International Conference on RF Superconductivity, pp. 347–349, JACoW Publishing, Geneva, Switzerland, 2015.

[47] J. Jonkers, M. Sande, A. Sola, A. Gamero, and J. Mullen, "On the differences between ionizing helium and argon plasmas at atmospheric pressure," *Plasma Sources Science and Technology*, vol. 12, p. 30, 12 2002.

[48] T. Powers, N. C. Brock, and T. D. Ganey, "In Situ Plasma Processing of Superconducting Cavities at JLab, 2023 Update," in *Proc. SRF'23*, no. 21 in International Conference on RF Superconductivity, pp. 701–705, JACoW Publishing, Geneva, Switzerland, 8 2023.

[49] P. Kolb *et al.*, "1.3 GHz Cavity Test Program for ARIEL," in *Proc. SRF'15*, no. 17 in International Conference on RF Superconductivity, pp. 350–354, JACoW Publishing, Geneva, Switzerland, 2015.

[50] W. Hartung *et al.*, "Investigation of Plasma Processing for Coaxial Resonators," in *Proc. SRF'23*, no. 21 in International Conference on RF Superconductivity, pp. 960–967, JACoW Publishing, Geneva, Switzerland, 8 2023.

[51] J. A. Bagger *et al.*, "ARIEL at TRIUMF: Science and Technology," in *Proc. IPAC'18*, no. 9 in International Particle Accelerator Conference, pp. 6–11, JACoW Publishing, Geneva, Switzerland, 2018.